Four-dimensional nuclear speckle phase separation dynamics regulate proteostasis

William Dion[1†], Heather Ballance[1†], Jane Lee[1], Yinghong Pan[2], Saad Irfan[1], Casey Edwards[1], Michelle Sun[1], Jing Zhang[1], Xin Zhang[3], Silvia Liu[4,5] and Bokai Zhu[1,4,6] *

[1]Aging Institute of UPMC, University of Pittsburgh School of Medicine; Pittsburgh, Pennsylvania, USA
[2]UPMC Genome Center; Pittsburgh, Pennsylvania, USA
[3]Department of Chemistry, the Pennsylvania State University, University Park, Pennsylvania, USA
[4]Pittsburgh Liver Research Center, University of Pittsburgh; Pittsburgh, Pennsylvania, USA
[5]Department of Pathology, University of Pittsburgh School of Medicine; Pittsburgh, Pennsylvania, USA
[6]Division of Endocrinology and Metabolism, Department of Medicine, University of Pittsburgh School of Medicine; Pittsburgh, Pennsylvania, USA

[†]These authors contributed equally to this work.

*Corresponding author. Email: bzhu@pitt.edu

Abstract:

Phase separation and biorhythms control biological processes in the spatial and temporal dimensions respectively, but mechanisms of four-dimensional integration remain elusive. Herein, we identified an evolutionarily conserved XBP1s-SON axis that establishes a cell-autonomous mammalian 12-hour ultradian rhythm of nuclear speckle liquid-liquid phase separation (LLPS) dynamics, separate from both the 24-hour circadian clock and the cell cycle. Higher expression of nuclear speckle scaffolding protein SON, observed at early morning/early afternoon, generates diffuse and fluid nuclear speckles, increases their interactions with chromatin in a proactive manner, transcriptionally amplifies the unfolded protein response, and protects against proteome stress; whereas the opposites are observed following reduced SON level at early evening/late morning. Correlative *Son* and proteostasis gene expression dynamics are further observed across the entire mouse lifespan. Our results suggest that by modulating the temporal dynamics of proteostasis, the nuclear speckle LLPS may represent a novel (chrono)-therapeutic target for pathologies associated with dysregulated proteostasis.

INTRODUCTION:

Most life on earth is governed by biological rhythms that are defined as self-sustained oscillations cycling with a fixed period. Biological clocks enable organisms to keep track of the time of day and to adjust their physiology to recurring daily changes in the external environment, including nutrient and microenvironment status. Our understandings of biological rhythms in mammals have expanded beyond the well-characterized circadian rhythms (~24h oscillation) in recent years through the discovery of 12h ultradian rhythms in mammals (*1, 2*). In contrast to earlier hypothesis that these 12h rhythms are under the combined regulation of the 24h circadian clock and feeding/fasting cues (*2, 3*), our group identified a cell-autonomous mammalian 12h ultradian oscillator that regulates 12h rhythms of systemic gene expression and metabolism (*4*). The 12h oscillator is independent from the 24h circadian clock, but instead regulated by the unfolded protein response (UPR) transcription factor spliced form of XBP1 (XBP1s) (*4-7*). In mouse, liver specific deletion of XBP1s impaired more than 80% of 12h transcriptome, while leaving the majority of circadian transcriptome intact (including all known core circadian clock genes) (*5, 6*). As a result of the 12h clock ablation, XBP1s liver-specific knockout ($XBP1^{LKO}$) mice exhibited drastically accelerated liver aging and fatty liver diseases (*5*).

Subsequent Gene Ontology (GO) analysis of XBP1s-dependent mouse hepatic 12h transcriptome revealed top-enriched genes involved in the entire central dogma information flow (CEDIF) process, ranging from transcription initiation, mRNA processing and export, ribosome biogenesis, translation initiation to protein folding, processing and sorting in the endoplasmic reticulum (ER) and Golgi, as well as various metabolic pathways including lipid and nucleotide metabolism (*6*). While the regulation of protein and lipid homeostasis by XBP1s is well-established (*8*), the control of mRNA metabolism by XBP1s and the mechanistic link between mRNA and protein homeostasis remain poorly characterized. Therefore, in this study, we aim to uncover the underlying mechanisms of coordinated mRNA and protein metabolism by investigating the 12h oscillator. By combining single cell time lapse microscopy, cistrome profiling and mathematical modeling, we unexpectedly identified an XBP1s-SON axis that dictates a cell-autonomous mammalian 12h ultradian rhythm of nuclear speckle liquid-liquid phase separation (LLPS) dynamics, which drives rhythmic global 12h nuclear speckle-chromatin interactions, uncoupled from the transcriptional state of individual genes. Very interestingly, we found that the expression of genes involved in proteostasis, including *Xbp1* itself, is hypersensitive to nuclear speckle LLPS dynamics change. We further observed correlative *Son* and proteostasis gene expression dynamics during the transient response to ER stress and across the entire mouse lifespan. Functionally, the XBP1s-SON axis can protect cells from proteome stress via transcriptionally amplifying the UPR. Our results thereby uncovered an intrinsic feedforward loop connecting nuclear speckle LLPS and proteostasis control that likely ensures a highly efficient genetic information transfer functioning at multiple temporal scales.

RESULTS:

XBP1s regulates a cell-autonomous 12h rhythm of nuclear speckle morphology change.

We first confirmed that the 12h rhythms of mRNA metabolic genes are also observed at the protein level by performing a *post-hoc* analysis of two published hepatic nuclear protein mass spectrometry datasets (*9, 10*) (fig. S1, A and B, and table S1). GO analysis of 12h nuclear proteins in both datasets revealed top enriched GO term ‘spliceosome’ (fig. S1C). Spliceosome is predominantly found in nuclear speckles, which are membraneless organelles enriched in pre-

mRNA processing factors, as well as various other proteins and non-coding RNAs (ncRNA) involved in RNA export, transcription regulation, pre-mRNA cleavage and polyadenylation and RNA degradation (*11, 12*). We further observed a robust 12h expression of nuclear speckle ncRNA *Malat1*, which is also a direct transcriptional target gene of XBP1s, and exhibits slightly dampened rhythm in XBP1 liver-specific knockout ($XBP1^{LKO}$) mice from our previously published RNA-seq dataset (*6*) (fig. S1, D and E).

To look for additional evidence of 12h mRNA metabolism besides gene expression, we initially asked whether the morphologies of nuclear speckle may exhibit time-of-the-day variation. Nuclear speckles normally are microscopically presented as "punctate" nuclear localization pattern, formed through liquid-liquid phase separation (LLPS) due to the prevalence of low complexity domains found in splicing factors (*11-13*). We performed immunofluorescence against SC35 (SRSF2), one well-established marker of nuclear speckles (*12, 13*), in the liver section of $XBP1^{Flox}$ and $XBP1^{LKO}$ mice at different CTs. Consistent with previous observations (*12, 14*), SC35 positive loci are associated with particularly low chromatin density, but in close proximity to chromatin, at all times in both $XBP1^{Flox}$ and $XBP1^{LKO}$ mice (fig. S2A). Nonetheless, we observed drastically distinct staining patterns of SC35 in $XBP1^{Flox}$ mouse liver at different times of day. At CT2, CT14, CT26 and CT38, spherical punctate patterns of SC35 found in the majority of nuclei are suggestive of LLPS formed via a process termed nucleation (*15*). By contrast, at CT8, CT20, CT32 and CT44, we observed a much more diffuse and network-like spatial distribution of SC35 staining, reminiscent of LLPS formed via spinodal decomposition (*15*) (Fig. 1A and fig. S2A). Quantifying these two distinct forms of LLPS by calculating the roundness of nuclear speckle staining as previously described (*16*) evinced an apparent 12h rhythm of nuclear speckle LLPS dynamics in $XBP1^{Flox}$ [p value of 0.032 by RAIN analysis (*17*)], but not in $XBP1^{LKO}$ mice (p value of 1 by RAIN analysis) (Fig. 1B), which is further confirmed by staining against a different nuclear speckle marker SON (p value of 0.031 and 0.54 in $XBP1^{Flox}$ and $XBP1^{LKO}$ mice by RAIN analysis, respectively) (fig. S2B).

To determine whether the 12h rhythm of nuclear speckle morphology change is cell-autonomous or not, we used CRISPR/CAS9 system to knock in GFP to the N-terminal region of endogenous SC35 locus in immortalized mouse embryonic fibroblasts (MEF) and performed time lapse imaging to track nuclear speckle morphology changes in single cells over time. This system allows us to probe nuclear speckle phase separation dynamics under physiological condition without the over-expression of speckle proteins. Western blot and immunofluorescence confirmed the successful generation of MEFs expressing GFP::SC35 fusion protein (fig. S2, C and D). In MEFs synchronized by serum shock, we observed robust in-phase ~12h rhythms of nuclear speckle morphology changes alternating between a high roundness punctate state and a low roundness diffuse state in single cells (Fig. 1, C and D, fig. S2E, and video S1). Interestingly, but consistent with our previous study (*4*), this 12h rhythm of nuclear speckle morphology changes are independent from the cell cycle (fig. S2, F and G). Even more intriguingly, in unsynchronized MEFs (no prior serum shock), we observed a weak local synchronization for cells within 140μm of each other, in terms of their nuclear speckle morphology oscillation (fig. S3, A to H), implying the very likely existence of paracrine factors for the local synchronization of 12h oscillator in adjacent cells *in vitro*.

Next, we used CRISPR/CAS9 to knock out the circadian clock master regulator BMAL1, or XBP1 in GFP::SC35 MEFs (fig. S4, A to C), and found that XBP1, but not BMAL1, is required for the establishment of the 12h rhythm of nuclear speckle morphology change (Fig. 1E). Since the ER-

localized endoribonuclease IRE1α can act both upstream (via alternatively splicing *Xbp1* mRNA to generate *Xbp1s*) and downstream (*Ire1α* mRNA exhibits XBP1s-depenent 12h rhythm) of XBP1s and was previously proposed to be an integral component of 12h oscillator regulatory network (fig. S5, A to C) (*7*), we further investigated whether IRE1α inhibition can also impair the 12h rhythm of nuclear speckle morphology change. Treating GFP::SC35 MEFs with the selective IRE1α inhibitor 4μ8c resulted in a low amplitude ~8h oscillation instead (fig. S5D). In summary, we therein demonstrated an IRE1α/XBP1s-dependent cell-autonomous 12h ultradian rhythm of nuclear speckle morphology that alternates between a more punctate and a more diffuse state. This 12h ultradian rhythm is further uncoupled from both the cell cycle and the 24h circadian clock, and exhibits local coupling in otherwise globally unsynchronized cells.

An evolutionarily conserved XBP1s-SON axis controls 12h rhythm of cell-autonomous nuclear speckle LLPS dynamics.

So, what may be the mechanism(s) underlying the observed 12h rhythm of nuclear speckle morphology change? A recent study on LLPS demonstrated that the concentration of scaffolding protein in the condensates can dictate the way by which LLPS occurs (*15, 18*). Simply put, under constant valency condition, a higher concentration of scaffolding protein (within the blue region of the phase diagram) will induce LLPS via spinodal decomposition (thus more diffuse), while a lower concentration (within the red region of the phase diagram) will lead to nucleation (thus rounder) (fig. S6, A and B). In nuclear speckles, the protein SON was previously hypothesized to act as a scaffolding protein upon which other RNA processing factors and ncRNA assemble (*19*). To test the idea that SON level may dictate nuclear speckle morphology, we first performed western blot analysis to examine the nuclear level of SON in the liver of wild-type mice at different times of day, and indeed observed a robust 12h oscillation of SON nuclear expression peaking at ~CT8, 20, 32 and 44 (Fig. 2, A and B, and fig. S6C). More importantly, the oscillation of SON is anti-phase with that of nuclear speckle sphericity, and the amplitude of physiological level of SON oscillation is two-to-three-fold change (Fig. 2, A and B). Both the phase and amplitude of 12h SON oscillation are consistent with the theoretical prediction by the LLPS phase diagram (Fig. 2, A and B, and fig. S6, A to C). The 12h rhythm of hepatic SON expression is further validated by the hepatic mass spectrometry dataset (*9*) (fig. S6, D and E). We next performed qPCR and identified a 12h rhythm of *Son* expression at the mRNA level in XBP1^{Flox} mice (Fig. 2C, and fig. S6F). By contrast, the period of *Son* mRNA oscillation was shortened to ~10h in XBP1^{LKO} mice (Fig. 2C, and fig. S6F). Cell-autonomous 12h *Son* mRNA expression is further identified in serum synchronized MMH-D3 hepatocytes *in vitro* (20), maintaining a similar relative phase to that of *Bmal1* as *in vivo* (fig. S6, G and H).

To determine whether *Son* is a direct transcriptional target gene of XBP1s, we first examined our previously published hepatic XBP1s ChIP-Seq dataset (*6*), and found a 12h XBP1s chromatin recruitment to the *Son* gene promoter region (fig. S6I). Consistent with the ChIP-Seq result, motif analysis scanning a 1kb region of the *Son* gene promoter further identified the XBP1s consensus binding sequence ACGTCA (fig. S6J). In addition, transient overexpression of XBP1s increased the expression of *Son* mRNA, together with canonical UPR genes *Manf* and *Hyou1* (fig. S6K). While these results strongly indicate that *Son* is under the direct transcriptional control of XBP1s, it is highly likely that additional transcriptional factors also regulate *Son* gene expression. In fact, our motif analysis also uncovered putative binding sites for GABPA and NFYA, two additional transcriptional factors involved in the 12h oscillator control (fig. S6J) (*Gabpa* and *Nyfa* themselves are also direct XBP1s transcriptional target genes) (*7*). The potential involvement of multiple

interlocked transcriptional loops in the regulation of *Son* gene expression is also likely responsible for its shortened ~10h period observed in XBP1^{LKO} mice, as previously seen in circadian period control (*21*).

We previously proposed that the mammalian 12h-clock likely evolved from the ancient circatidal clock of marine animals, who adapt their behaviors to the ~12h ebb and flow of the tides resulting from the gravitational pull of the moon (*1, 22*). Evidences supporting this evolutionary origin include conserved 12h rhythms of gene expression between mice and two marine species, the sea anemone *Aiptasia diaphaha* and the limpet *Cellana rota* (*6*). In line with this evolutionary conservation, we observed robust 12h rhythms of mRNA expression of *Son* orthologs in *Aiptasia diaphaha* (*23*) and *Cellana rota* (*24*) (Fig. 2, D and E). As a matter of fact, mRNA processing is the most enriched biological pathway associated with circatidal genes in both marine animals (*6*). Since 12h rhythm of *Xbp1* expression was previously found to be also conserved in marine species (*1*), these results indicate that the 12h rhythm of XBP1s-SON axis is evolutionarily conserved.

To establish the causality between SON expression and nuclear speckle morphology, we knocked down or overexpressed SON by siRNA or the CRISPR/dCAS9-VPR (*25*) system in GFP::SC35 MEFs, respectively (fig. S7, A to F). As expected, both manipulations impaired the 12h rhythm of cell-autonomous nuclear speckle morphology change, with the former increasing (Fig. 2, F to H, fig. S7C) and the latter decreasing (fig. S7G) the average roundness of nuclear speckles, again in line with the theoretical prediction by the LLPS phase diagram. This morphology change is ostensibly reversible, as in the later days of imaging, the 12h rhythm of nuclear speckle morphology change is restored, likely due to the gradual loss/dilution of *Son* siRNA (Fig. 2H). To determine whether the morphology changes of nuclear speckle are associated with fluctuations in its dynamics, we performed Fluorescence Recovery after Photobleaching (FRAP) in GFP::SC35 MEFs, and found that SON positively regulates the fluidity of nuclear speckles (Fig. 2, I and J, fig. S7, H and I, videos S2, and S3). We further observed a very robust 12h rhythm (with a range of ~8 to ~32 s of recovery half-life) of nuclear speckle fluidity in serum shock-synchronized GFP::SC35 MEFs, well in line with the 12h rhythm of nuclear speckle sphericity, with decreased fluidity (longer recovery half-life) coinciding with rounder nuclear speckles (sphericity approaching 1) (Fig. 2K). Thus far, we have demonstrated an evolutionarily conserved XBP1s-SON axis that controls a 12h rhythm of cell-autonomous nuclear speckle liquid-liquid phase separation dynamics: a higher level of SON expression, observed at early afternoon (CT8) and early morning (CT20), leads to a more diffuse and fluid nuclear speckle morphology, while a lower SON expression, seen at early evening (CT14) and late morning (CT2), renders nuclear speckles to a more spherical and more stagnant state.

XBP1s regulates 12h rhythmic nuclear speckle-chromatin interactions.

Next, we wondered whether these observed nuclear speckle condensates dynamics lead to a change in their spatial distribution, more specifically, their propensity to associate with chromatin. To detect temporal nuclear speckle-chromatin interactions, we performed ChIP-Seq in the liver of XBP1^{Flox} and XBP1^{LKO} mice at 4h interval for two days at constant darkness, using a mono-clonal antibody against mouse SC35 (SRSF2), which has recently been successfully used to characterize splicing condensates-chromatin interactions (*26*). Consistent with previous SC35 ChIP-seq and *Malat1* CHART-Seq results (*26, 27*), nuclear speckle-chromatin interactions are enriched in gene bodies, with a gradual increase in binding intensity toward the 3' transcription termination site (TTS), as exemplified by very strong binding observed at *Neat1* and *Malat1*

themselves as expected (Fig. 3A and fig. S8A). Very intriguingly, we observed a dominant global 12h rhythm of nuclear speckle-chromatin interactions in XBP1^{Flox} mice cresting at CT8, CT20, CT32, and CT44 (Fig. 3A and fig. S8, A to F), which corresponds to peaking SON expression and nuclear speckle fluidity and diffuseness at the same time (Fig. 1, A and B, and Fig. 2, A and B). We identified a total of 5,365 genes in wild-type mice that have high confidence nuclear speckle-chromatin interactions within gene bodies, and 3,027 of them have robust ~12h rhythmic nuclear speckle-chromatin interaction [with a false discovery rate (FDR) cut-off of 0.2 by RAIN analysis] (Fig. 3A and tables S2 and S3). These genes are very strongly enriched in metabolic and protein homeostasis/ER stress pathways (Fig. 3B). Although below detection threshold for peak-calling algorithms, weaker 12h rhythmic nuclear speckle-chromatin interactions were also observed in an additional 4,130 genes by the eigenvalue/pencil method (*4, 28*) (table S4, fig. S8, B, D and F), which together with the 3,027 genes account for more than half of all expressed genes in the wild-type mouse liver. In contrast, ~12h rhythms of global nuclear speckle-chromatin interactions were significantly impaired in XBP1^{LKO} mice. Instead, a low amplitude ~10h global binding rhythm was observed after polynomial detrend (Fig. 3A, fig. S8, A to G and table S4). Of note, this rhythmicity is in line with the ~10h *Son* mRNA oscillation observed in XBP1^{LKO} mice liver (Fig. 2C and fig. S6F).

To determine if the rhythmic nuclear speckle-chromatin interactions are correlated with transcriptional state fluctuations in mouse liver *in vivo*, we estimated the temporal pre-mRNA and mature mRNA level of each hepatic gene by respectively quantifying the reads mapped to intron and exon regions, using our previously published RNA-seq dataset (*6*) (Fig. 3C and tables S5 and 6). Consistent with past studies (*12, 13, 29*), on a global scale, higher daily-average nuclear speckle-chromatin recruitment is strongly associated with higher daily-average gene expression in both XBP1^{Flox} and XBP1^{LKO} mice (fig. S9A). However, on an individual gene level, temporal rhythmic nuclear speckle-chromatin interaction is largely decoupled from temporal gene expression, as not all nuclear speckle-associated genes exhibit 12h rhythms of expression (Fig. 3D). We further estimated the mRNA processing rate of each gene via a simple first-order kinetic model of transcription regulation (*30*) (assuming the mRNA degradation rate remains constant during a day), and found a strong positive correlation between 12h rhythmic nuclear speckle-chromatin association and 12h rhythmic mRNA processing rate in XBP1^{Flox} mice that both peak around CT8/CT20 (Fig. 3, C to G, and fig. S9B). Compared to XBP1^{Flox} mice, the daily-average mRNA processing rate in XBP1^{LKO} mice liver was slightly reduced (fig. S9C), and exhibited a dominant population of shortened ~10h oscillations (Fig. 3D and fig. S9D), again in line with observed ~10h rhythm of *Son* expression (Fig. 2C and fig. S6F) and ~10h oscillation of nuclear speckle-chromatin interactions (fig. S8, F and G). For those genes that do maintain ~12h mRNA processing rate in XBP1^{LKO} mice, they have lower amplitude compared to wild-type counterparts (Fig. 3F) and a more diffuse phase distribution (Fig. S9E). 12h rhythmic nuclear speckle-chromatin interaction and subsequent 12h mRNA processing rates significantly contribute to the establishment of 12h rhythm, but not 24h circadian rhythm of gene expression post-transcriptionally in XBP1^{Flox} mice (Fig. 3H), with examples of *Rela* and *Id1* genes only exhibiting 12h rhythms at the mature mRNA level in XBP1^{Flox} mice (Fig. 3, I to K, and fig. S9, F to H). As a matter of fact, dominant 24h circadian rhythms of nuclear speckle-chromatin interactions and mRNA processing rates were observed on all core circadian clock genes with similar amplitudes in both XBP1^{Flox} and XBP1^{LKO} mice, in phase to their respective temporal gene expression profile (fig. S10, A to D), although some genes (such as *Per1* and *Nfil3*) have weaker superimposed 12h rhythmic nuclear speckle-chromatin interactions (also peaking at CT8/CT20), which are lost in

XBP1^{LKO} mice (fig. S10C). Since the core circadian gene expressions are not altered in XBP1^{LKO} mice (*6*), these results suggest that the SON-mediated 12h rhythmic nuclear speckle-chromatin interactions are largely dispensable for the establishment of 24h core circadian clock gene expression in mice.

Proteostasis gene expressions are hyper-sensitive to nuclear speckle LLPS dynamic change.

Focusing on 528 genes that exhibit very robust 12h rhythms of nuclear speckle-chromatin interactions (FDR = 0.2 among the 5,365 genes with strong SC35 binding peaks) as well as XBP1s-dependent 12h rhythms of gene expression (FDR = 0.2 at both the pre and mature mRNA level) (fig. S11, A to D), we identified two major groups of genes with different phase relationship between the two. For 260 genes enriched in lipid metabolism and PPAR signaling (blue area in Fig. 4, A and B), nuclear speckle-chromatin interaction peaks at CT8, closely following the peak of nascent mRNA expression at CT6 and matches the peak of mature mRNA expression (fig. S11, E and F). Very intriguingly, for the majority of 130 genes enriched in ER stress and protein sorting pathways (red area in Fig. 4, A and B), the peaking times of the nuclear speckle-chromatin interactions precede those of nascent mRNA expression (above the diagonal line in Fig. 4A), which include genes like *Manf*, *Hyou1* and *Sec23b* (Fig. 4A). In fact, for 69 genes with additional 12h XBP1s chromatin recruitment (*6*), the acrophase of nuclear speckle-chromatin interaction can even precede that of XBP1s chromatin binding, with *Xbp1* itself as a good example (Fig. 4C and fig. S11, G and H).

These results imply the existence of multitiered mechanisms for regulating nuclear speckle-chromatin interactions. As recently demonstrated, nuclear speckle condensates are thought to be "passively" recruited to chromatin following nascent mRNA transcription, mediated by RNA polymerase II hyper-phosphorylation during transcriptional elongation (Fig. 4D-i) (*26*). This mechanism is likely responsible for maintaining the core circadian clock and lipid metabolism gene expression, as the dynamics of their nuclear speckle-chromatin interactions closely follow their temporal gene expression change. The emerging data further suggests an additional layer of nuclear speckle-chromatin interaction control. Rather than responding to the transcriptional state of individual genes, nuclear speckle-chromatin interactions can also be modulated by the SON-mediated nuclear speckle LLPS dynamics on a global scale (Fig.4D, ii and iii). In this case, the dynamics of nuclear speckle-chromatin interactions can even precede the subsequent gene expression change. The new data further suggests that this second mode of "proactive" nuclear speckle-chromatin interaction is strongly implicated in the transcription regulation of proteostasis and UPR genes.

SON transcriptionally amplifies the UPR and protects against proteome stress.

Before the discovery of the mammalian 12h oscillator, UPR was classically studied as a transient response to an insult to the ER (also known as ER stress). Transmitting a cascade of signals from ER to the nucleus, UPR ultimately activates three main transcription factors XBP1s, ATF4 and ATF6 (*31*). To seek more support for the causal role of SON and nuclear speckle LLPS on UPR gene regulation, we further examined the temporal kinetics of canonical UPR in response to a very low dose of ER stress inducer tunicamycin (Tu) (100ng/ml) in MEFs. We noted that starting from 2 hours after Tu treatment, an immediate early increase of SON expression was concomitant with increasing nuclear speckle fluidity and diffuseness and increasing nuclear speckle-chromatin interactions in the gene bodies and/or transcription termination sites of *Xbp1*, *Manf*, and *Hyou1*

genes (Fig. 5, A to D). More importantly, this immediate early SON-mediated nuclear speckle LLPS dynamics change precedes the increase of XBP1s promoter recruitment as well as *Xbp1*, *Manf* and *Hyou1* gene expression with a phase advance of ~3.3h (Fig. 5, B to D), similar to what was observed in mouse liver *in vivo* (fig. S6E). We further observed a second wave of nuclear speckle-chromatin interactions peaking at 8 hours after Tu treatment that follows XBP1s promoter recruitment (Fig. 5D). This second wave is not associated with increased nuclear speckle fluidity, and thus reflects "passive" chromatin recruitment of nuclear speckles during transcription elongation (Fig. 5A). This reduced nuclear speckle fluidity during the second wave is likely a result of a more stable interaction between nuclear speckle and chromatin during mRNA processing.

To confirm the ChIP-qPCR results, we performed immunofluorescence and observed a dose-dependent increase of co-localization of XBP1s with nuclear speckles in response to ER stress in MEFs (fig. S12, A to D). Importantly, siRNA-mediated knocking down of SON significantly reduces ER stress-induced nuclear speckle-chromatin interactions (Fig. 6A), disrupts XBP1s and nuclear speckle co-localization (Fig. 6B), and subsequently greatly blunts Tu-induced UPR at both the pre and mature mRNA level, while not affecting core circadian clock genes expression (Fig. 7A and fig. S13, A and B). By contrast, both stable and transient dCAS9-VPR-mediated overexpression of endogenous SON significantly amplifies UPR at the transcriptional level (Fig. 7B and fig. S13, C to F). UPR genes under SON control include not only ER stress-responsive output genes such as *Manf* and *Hyou1*, but also core regulatory genes in the XBP1 and ATF4 branches of the UPR: *Xbp1* itself, *Ire1α* and *Atf4* (Fig. 7, C to H), the latter of which appears to respond to a narrower range of SON level, as overexpression of SON has little effect on *Atf4* gene expression (Fig. 7F). By contrast, SON does not significantly affect *Atf6* expression (Fig. 7, C and F). The dichotomy of the effects of SON on *Atf4* and *Atf6* gene expression during transient ER stress in MEFs is consistent with their differential temporal gene expression profiles in mouse liver *in vivo*: while both *Atf4* and *Atf6* pre-mRNA exhibit 12h rhythms in wild-type mouse liver, only the former exhibits a robust 12h rhythm of XBP1s-dependent nuclear speckle-chromatin interaction and dampened 12h rhythm of expression in XBP1 ^{LKO} mice (fig. S13, G to J). These UPR gene expression changes in response to SON manipulation are similarly conserved at the protein level (Fig. 7, D, E, G and H) and largely recapitulated with a different ER stress inducer DTT (fig. S14, A and B). Finally, we ruled out the possibility that protein synthesis is involved in the transcriptional regulation of the early stage of UPR by SON, as neither changes of protein synthesis rate (fig. S15, A and B) nor the relative amount of phospho-PERK (Thr980) levels (Fig. 7, D, E, G and H) were observed under SON knocking down or overexpression conditions. Taken together, our data strongly indicate that SON can rapidly amplify XBP1s and ATF4 (although to a lesser extent)-mediated UPR, while having very modest effects on the ATF6 branch at the transcriptional level.

To determine the functional importance of SON in regulating proteostasis in the ER, we went on to detect and quantify ER proteome stress in response to SON manipulation in MEFs. We utilized a previously published Halo-tag mutant (K73T/L172Q) prone to ER-localized aggregation ($AgHalo_{ER}$) (*32*). The $AgHalo_{ER}$ sensor was labeled with solvatochromic fluorogenic probe (P1), which turns on fluorescence only upon its misfolding and aggregation (*33*). As expected, live cell imaging of MEFs expressing $AgHalo_{ER}$ labeled by P1 probe demonstrated that the $AgHalo_{ER}$ was well-folded with little green fluorescence signal under basal conditions and formed granular green fluorescent structures after 16h Tu treatment (Fig. 8A). More importantly, under both basal and Tu conditions, a significant increase of $AgHalo_{ER}$ staining intensity was observed in SON-depleted MEFs (Fig. 8, A and B), which is concomitant with reduced cell number in response to a higher

concentration of Tu treatment under SON-depleted condition (Fig. 8C). Conversely, dCAS9-VPR-mediated SON overexpression significantly reduced $AgHalo_{ER}$ misfolding and protected against ER stress-induced cell death (Fig. 8, D to F). Collectively, these data indicate that by amplifying the UPR, SON can protect cells against proteome stress.

Consistent with its role in amplifying UPR during transient ER stress, *Son* knock-down further dampened the 12h oscillation of *Manf* promoter-driven luciferase activity, while having no apparent effects on circadian *Bmal1* promoter-driven luciferase rhythm (fig. S16, A to F). Together, these results strongly support a positive causal role of SON and nuclear speckle LLPS on the transcriptional regulation of proteostasis, both for UPR in response to a transient ER stress and the cell-autonomous 12h oscillator.

Correlative SON and UPR gene expression dynamics across mouse life span.

To determine whether the hourly *Son* and UPR gene expression dynamics can be extrapolated to a longer temporal scale, we analyzed a recently published RNA-seq data in multiple mouse tissues across a 27-months lifespan (*34*). We observed strong correlative *Son* and UPR mRNA expression dynamics in the liver, skin, heart, pancreas and bone across the entire mouse lifespan (Fig. 9, A and B, and fig. S17, A to D). In addition to the liver, 12h rhythms of *Son* and UPR mRNA were also observed in mouse skin (*35*), heart (*36*) and pancreas (*37*) (fig. S17, A to C), with the latter exhibiting a very intriguing fractal feature of anti-phase oscillations of *Son* and UPR gene expression at the periods of 12h and ~16 months (fig. S17C). The anti-correlation between *Son* and UPR mRNA in mouse pancreas could be due to a large discordance between the mRNA and protein level of SON and warrants further investigation. In contrast to UPR genes, no strong correlation was observed between the gene expression dynamics of *Son*, and lipid and core circadian clock genes in different tissues across the mouse lifespan (Fig. 9, A and B, and fig. S17, A to D).

Discussions:

While considerable progress has been made towards understanding the biophysical properties and the biological functions of biomolecular condensates and LLPS (*38*), it remains elusive whether LLPS dynamics are under the control of “autonomous clocks” (*39*). Our study hereby demonstrates the existence of an evolutionarily conserved XBP1s-SON axis that integrates the 12h oscillator with nuclear speckle LLPS to spatiotemporally program proteostasis (Fig. 10). As the scaffolding protein of nuclear speckle condensates (*19*), SON level can dictate the mechanisms by which nuclear speckles phase separate. Nuclear speckles with a lower concentration of SON exhibit features reminiscent of punctate nucleation and growth, while those with higher SON expressions exhibit early stage coarsening morphologies—connected network-like condensates—associated with spinodal decomposition (*15*). While the coarsening of condensates will eventually result in the coalescence of all droplets into a single large sphere in an ideal situation driven by surface tension, the chromatin likely greatly slows down this process so that an intermediate connected network-like nuclear speckle morphology can occur (*40*). Both the phase and amplitude of SON oscillation further align with the prediction by the phase separation diagram. More fascinatingly, nuclear speckles with lower SON expression are also more stagnant, whereas much more fluid dynamics are found in nuclear speckles with higher SON expression. Whether the dynamics of nuclear speckles LLPS is intrinsic to the way by which LLPS occurs (nucleation or spinodal decomposition) remains to be determined. One possibility is that nucleation-mediated LLPS will result in many individually isolated condensates and the

barriers of liquid droplets would limit molecular diffusion between dense and dilute phases, while during spinodal decomposition, the connected network-like condensates morphology would greatly favor rapid molecular diffusion within the condensates. The latter would also facilitate the rapid delivery of splicing factors to transcription foci during ER stress to amplify the UPR at the co-transcriptional splicing/transcription elongation stage (*18*). Conversely, lower SON expression-associated stagnant nuclear speckles are sequestered away from chromatin and thereby would greatly dampen the UPR (Fig. 4D and 10). It is worth noting that besides SON, we are not ruling out the possibility that other nuclear speckle proteins and/or RNAs may also regulate the 12h nuclear speckle LLPS dynamics, with the Pickering agent, which has recently been found to be regulating P granules coarsening, being a tantalizing candidate (*41*). Our results further reconcile the debate on the exact roles of nuclear speckles in gene regulation: whether the nuclear speckles mainly function as the 'storage facility' of mRNA processing factors away from chromatin, or they can actively participate in gene regulation process via physical engagement with chromatin (*42*). We showed here that nuclear speckles can function as both, but these two functions are probably temporally separated due to the oscillation of SON expression and the according changes in their LLPS dynamics and propensity to associate with chromatin.

So, what could be the biological advantages of having a 12h rhythm of nuclear speckle LLPS dynamics? Since the acrophases (the time period in a cycle during which the cycle peaks) of 12h rhythms of gene expression are strongly biased toward dawn and dusk, we previously proposed a vehicle-cargo hypothesis to elucidate the distinct functions of 12-hour versus the circadian rhythms (*6*). We argued that the 12-hour rhythm accommodates increased demands for gene expression/processing at the two biological 'rush hours' (dawn and dusk) by elevating the global traffic capacity of the central dogma information flow. This connects and tunes rates of mRNA, protein and lipid metabolism to the 12-hour cycle of metabolic stress (thus acting as the vehicle). The circadian clock, on the other hand, dictates the particular genes/gene products processed at each rush hour (thus acting as the cargo). We posit that having increased nuclear speckle fluidity at early morning/early afternoon enables the in-land animals to anticipate, and subsequently to rapidly turn on UPR genes to cope with heightened metabolic stress associated with transition periods later at dawn and dusk. This feature is likely co-opted from the circatidal clock of marine animals, who probably used a similar system to adapt to the 12h environmental cues resulting from tidal changes. The hypersensitivity of proteostasis gene expression to nuclear speckle LLPS dynamics would ensure tightly coupled mRNA and protein metabolic processes, which in turn can entail a highly efficient genetic information transfer across multiple compartments within the cell. The fact that manipulating the liquid-liquid phase separation dynamics of nuclear speckle is sufficient to alter the transcriptional output of proteostasis genes further suggests that the nuclear speckle LLPS may represent a novel (chrono)-therapeutic target for pathologies associated with dysregulated proteostasis (Fig. 10). Interestingly, a recent study found that the nuclear speckle can also amplify p53-mediated gene expression (*43*). Since p53 is known to be part of the DNA damage response, it is reasonable to conjecture that boosting nuclear speckle function via modulating its LLPS may exert beneficial effects via simultaneously augmenting multiple adaptive stress responses, thereby potentially enhancing the overall anti-aging hormesis (*44*).

On a more philosophical note, our study is a good example of how seemingly unrelated biological processes can in fact be tightly connected through the time dimension, in this case their 12 hour of rhythmicity. In this study, we showed that one can use frequency spectrum similarity to interrogate genetic interactions within a cell. We hope that our study will make the scientific community think more deeply about the temporal dimension of their biological problems and

facilitate the achievement of the ultimate goal of "mapping the four-dimensional atlas" of biological processes.

MATERIALS AND METHODS

Animals

XBP1^{Flox} mice was previously described (*45*). XBP1^{LKO} mice were generated by crossing Albumin-CRE mice with XBP1^{Flox} mice. All mice are in C57BL/6 background, male and between 3 and 4 months of age. Mice were first entrained under LD12:12 conditions for 2 weeks before transferred to constant darkness for 24hrs. Mice were then sacrificed at a 2h interval for a total of 48 hrs. Mice were fed *ad libitum* during the entire experiment. The animal studies were carried out in accordance with the National Institutes of Health guidelines and were granted formal approval by the University of Pittsburgh's Institutional Animal Care and Use Committee (approval number IS00013119 and IS00013119).

Plasmids

Mouse non-targeting, *Bmal1* and *Xbp1* sgRNAs were cloned into the lentiCRISPRv2 plasmid as previously described (*46*), which is a gift from Dr. Toren Finkel. The sgRNA sequences (**in bold**) are as follows: Non-targeting control*:* caccg**AAATGTGAGATCAGAGTAAT**; *Bmal1*: caccg**CCCACAGTCAGATTGAAAAG**; *Xbp1*: caccg**GGAGCAGCAAGTGGTGGATT**. dCAS9-VPR plasmid (*47*) was a gift from George Church (Addgene plasmid # 63798; http://n2t.net/addgene:63798 ; RRID:Addgene_63798). Mouse non-targeting, *Son* promoter-targeting sgRNAs were cloned into the pLenti-SpBsmBI-sgRNA-Hygro plasmid (*47*), which was a gift from Rene Maehr (Addgene plasmid # 62205; http://n2t.net/addgene:62205; RRID: Addgene_62205). The sgRNA sequences are as follows: Non-targeting control*:* aaatgtgagatcagagtaat; *Son* promoter-targeting sgRNA1: atggcggccgagttcgtgcg; *Son* promoter-targeting sgRNA2: taggagtccccgcaggctga. XBP1s over-expression plasmid PHAGE-Flag-XBP1s was previously described (*4*).

siRNA/sgRNA Transient Transfections

MEFs were transfected with 10μM of different siRNAs for 24~48 hours with Lipofectamine RNAiMAX reagents (Life technologies) per the manufacturer's instructions. Source of siRNA are as follows: siGENOME Non-Targeting siRNA pool (Dharmacon, D-001206-1305), siGENOME SMARTpool SON siRNA (Dharmacon, L-059591-01-0005). For transient transfection of son promoter-targeting sgRNAs, non-targeting sgRNA or *Son* promoter-targeting sgRNA1 and sgRNA2 were synthesized *in vitro* by EnGen® sgRNA Synthesis Kit, *S. pyogenes* per manufacture's protocol. MEFs stably expressing dCAS9-VPR were transfected with 10μM of different sgRNAs and co-treated with 100ng/ml of tunicamycin for 6h.

Cell culture

MEFs were isolated from male SRC-2$^{fl/fl}$ mice and immortalized by SV40 T antigen as previously described (*48*). For dexamethasone treatment, MEFs were cultured in DMEM (4.5g/L glucose) supplemented with 10% FBS and treated with 100nM Dex for 30mins, and then washed with 1X PBS before cultured in the same medium. For serum shock, MEFs were cultured in DMEM (4.5g/L glucose) supplemented with 10% FBS and treated with 50% horse serum for 2h, and then washed with 1X PBS before cultured in the same medium. For tunicamycin treatment, MEFs were treated

with 100ng/ml tunicamycin (in DMSO) for different times, unless it is otherwise indicated. For all cell culture experiments, cells were cultured at 37 °C with 5% CO2.

Establishing stable cell line

For sgRNA-mediated Bmal1/XBP1 knock-out MEFs, lentiviruses packaged in HEK293T cells with co-transfection of lentiCRISPRv2, pMD2.G and psPAX2 plasmids were used to infect MEFs with a multiplicity of infection (MOI) of 3. Stable MEFs were selected in the presence of 4μg/ml of puromycin. For SON trans-activation MEFs, MEFs were first transfected with dCAS9-VPR plasmid, and those stably-expressing dCAS9-VPR were selected in the presence of 200μg/ml of G418. dCAS9-VPR stably-expressing MEFs were further infected with lentiviruses packaged from HEK293T cells transfected with pLenti-SpBsmBI-sgRNA-Hygro, pMD2.G and psPAX2 plasmids. Final SON trans-activation MEFs (with *Son* promoter-targeting sgRNA1) were selected in the presence of 200μg/ml of G418 and 200μg/ml hygromycin.

Generation of GFP::SC35 cells

The CRIS-PITCh (v2) system as described in (*49*) were used to generate an GFP::SC35 knock-in cell line. The CRIS-PITCh (v2) system requires an "All-in-one" expressing CAS9, a CRISPR guide strand targeting a cut site in the desired genomic locus and a CRISPR guide strand targeting the CRIS-PITCh (v2). The CRIS-PITCh (v2) contains a sequence designed to recombine into the desired locus and insert a sequence (Puro-T2A-EGFP). All-in-one vector: Oligos (ThermoFisher) Fwd 5'CACCTGTCCGGGGCGTTAGGGTCT 3' and Rev 5'-AAACAGACCCTAACGCCCCGGACA-'3 were annealed using Nuclease Free Duplex Buffer (IDT 11-01-03-01). The plasmid pX330_1x2_addgene-58766-sequence-202009 (Addgene, https://www.addgene.org/58766/), was digested with BbsI-HF (NEB R3539S) (Antarctic Phosphatase M0289S) and gel purified. The resulting fragment was ligated to the annealed oligos using T4 ligase (M0202S). The Pitch guide RNA was cleaved form the Pitch_Cas9_addgene-63670-pX330S-2-Cas9PITCh-106070 (Addgene, http://www.addgene.org/browse/article/16395/)plasmid using BsaI-HF®v2 (NEB, R3733S). This fragment was gel purified and ligated to BsaI BsaI-HF®v2 (NEB, R3733S) cleaved and purified SRSF2 guide RNA vector. The resulting vector contained sequences to express the SRSF2 locus specific guide RNA as well as the Pitch guide RNA. CRIS-PITCh (v2): The Puro-T2A-EGFP region was amplified from the mp132-psicor-puro-t2a-egfp plasmid (ViraCore at UCSF, viracore.ucsf.edu) using the following primers (ThermoFisher), and Q5® High-Fidelity 2X Master Mix (NEB, M0492S): Fwd: 5'-CCGCGTTACATAGCATCGTACGCGTACGTGTTTGGTGTCCGGGGCGTTAGGGTCTATGAC CGAGTACAAGCCC-3' Rev: 5'-CAGCATTCTAGAGCATCGTACGCGTACGTGTTTGGGGCGGGCGGCCGTAGCTCATGGATC CGGGCTTGTACAGCTCGTCCATG-3' The resulting PCR fragment was gel purified and joined to the MluI (NEB, R0198S) digested pCRIS-PITChv2-FBL (http://www.addgene.org/63672/) using Gibson Assembly (NEB R3539S). 1.2 μg of the All-in-one vector and 0.6 μg of the CRIS-PITCh (v2) in were transfected into a 100 mm dish of low-passage number mouse embryonic fibroblasts using LipofectamineTM 3000 (Invitrogen, 100022052) and P3000TM Reagent (Invitrogen 100022058), and Optimem (Gibco, 31985-070). The transfected MEFs were cultured (DMEM (Gibco, 21013-024), 10% FBS (HyClone SH30910.03), 1% Pen-Strep (Gibco, 15140-122), 1% Sodium Pyruvate (Gibco, 11360-070)) in increasing concentrations (2 -5 ug/mL puromycin (Gibco A11138-03)) for selection. Colonies were diluted using 15 cm cell culture plates. Colonies were

examined for EGFP fluorescence, and were subsequently cloned using cloning circles (Sigma, Z370789) and Trypsin EDTA (Gibco, 25200072).

Real-time Luminescence Assay

Stable *Manf*-dluc (*6*) or *Bmal1*-dluc MEFs (*6*) were cultured in DMEM (4.5g/L glucose) supplemented with 10% FBS and treated with 50% horse serum in DMEM for 2h or or 100nM for 30mins before subjected to real-time luminescence assay using a Lumicycle (Actimetrics) as previously described (*6*). Briefly, after serum shock treatment, MEFs were washed with 1x PBS and cultured with DMEM (4.5g/L glucose) supplemented with 0.1 mM Luciferin and 10mM HEPES buffer in 35 mm tissue culture dishes in the absence of serum and transferred immediately to Lumicycle for real-time luminescence analysis. Periods of oscillation were identified by embedded Periodogram function. For siRNA treated MEFs, MEFs were transfected with non-targeting or *Son* siRNA for 48 hours before subject to serum shock and real-time luminescence assay as described above.

Immunofluorescence

Immunofluorescence was performed as previously described (*50*). Briefly, liver OCT sections or cells cultured in chamber slide were fixed in cold acetone for 10 mins at -20 ºC. The sections were then air dried, rehydrated with PBS and permeabilized with PBS+ 0.1% Triton X-100. The sections were then blocked with 10% goat serum at room temperature for 1 hour. Primary antibodies against SC35 (ab11826, Abcam), XBP1s (Biolegend 658802) and SON (abcam 121033) was conjugated to Alexa-488 or Alexa-555, respectively per manufacture's protocol and added to the OCT section at 1:1000 dilution overnight at 4 ºC. Next day, sections were washed five times with PBS and counterstained with DAPI before mounting (with ProlongGold Glass) and imaging using Leica SP8 lightening confocal microscope (Leica Microsystems). 3D construction from z-stack images was performed using Volume Viewer from Image J.

Image analysis

All image analysis were performed in Cell Profiler (version 3.1.5). Quantification of the shape of nuclear speckles was performed with customarily-written pipelines in Cell Profiler. For speckle *i* the sphericity is defined as equation 1:

$$\text{Sphericity } i = 2\sqrt{\pi} * \sqrt{\text{area } i} \div \text{circumference } i \quad (1)$$

So that a perfect circle will have a sphericity of 1, and a line will have a sphericity of 0. To calculate the average sphericity of a single cell that have *k* speckles, we calculated the area-weighted average as described in equation 2.

$$Average\ sphericity/cell = \sum_1^k Sphericity\ i \times area\ i \,/\, \sum_1^k area\ i \quad (2)$$

Time-lapse Microscopy

Time-lapse imaging was performed using SP8 lightening confocal microscope (Leica Microsystems) with Okolab stage top incubator to maintain constant CO_2 (5%), temperature (37 ºC) and humidity (90%). Cells were plated into 8-well chamber slide in full DMEM media and images were taken every 15 minutes using autofocus function. For imaging of cells in multiple wells simultaneously, Mark and Find feature was used to ensure accurate capture of the same cells.

Fluorescence Recovery After Photobleaching (FRAP)

FRAP was performed using Leica SP8 lightening confocal microscope (Leica Microsystems) with 488-nm laser. Bleaching was performed using 100% laser power with 3.6 microseconds/pixel dwell time for 5 cycles, and images were collected every 1.29 second for 50 frames post-bleaching. Fluorescence intensity at the bleached spot, a control unbleached spot and background was measured using the embedded FRAP Profiler. Background intensity was subtracted, and values are reported relative to the unbleached spot to control for photobleaching during image acquisition. The recovery half-life ($t_{1/2}$) was calculated by the online easyFRAP tool (*51*) (https://easyfrap.vmnet.upatras.gr/) by fitting to single or double exponential equations with the better fit (larger R square values). For temporal FRAP analysis, different cells were selected for FRAP at each time point after Tu treatment or serum synchronization to minimize photo-toxicity to cells due to repeated photobleaching.

ER proteostasis assay

MEFs were seeded in an 8-well chamber slide and transiently transfected with plasmid expressing CMV promoter-driven ER-localized aggregation-prone Halo-tag mutant (K73T/L172Q) ($AgHalo_{ER}$) (*32*). After 24 hours, the same cells were transfected with scrambled or *Son* siRNA for another 24 hours. Then cells were treated with DMSO vehicle control, 50ng/ml or 100ng/ml Tu for 16 hours. After that, cells were replaced with fresh DMEM medium containing 1μM P1 to label $AgHalo_{ER}$ protein for 30 min, and then co-stained with Hoechst 33342/DAPI for nuclei. dCAS9-VPR GFP::SC35 MEFs expressing control or *Son* promoter-targeting sgRNA were transiently transfected with $AgHalo_{ER}$ plasmid and then treated with 100ng/ml Tu for 16h before subject to confocal live imaging. Confocal images were obtained using a Leica SP8 confocal microscope (Leica Microsystems). The P1 signal was visualized with a blue argon laser (488 nm), and the Hoechst/DAPI signal was visualized using an ultraviolet laser (405 nm). Quantification of intensity was performed with Cell Profiler (version 3.15). For GFP::SC35 MEFs, only green signals that don't overlap with Hoechst staining (nucleus) were quantified.

Quantification of protein synthesis rate

The Click-iT HPG Alexa Fluor 594 protein synthesis HCS kit (Thermo) was used to measure protein synthesis in vitro. Briefly, MEFs cultured in chamber slides were treated with DMSO or 100ng/ml Tu for 5.5h before being pulsed with 50 μM methionine analog L-homopropargylglycine in methionine-free medium for 0.5 h. Cells were fixed with 2% formaldehyde and permeabilized by 0.5% Triton X-100 and then underwent a ligation reaction for 30 minutes in the dark. Nuclei were further counterstained with Hoechst. Representative photomicrographs were obtained with a Leica SP8 confocal microscope (Leica Microsystems), and cell average intensity of Alexa-594 signal was measured using Cell Profiler software (version 3.15). Only cytosolic Alexa-594 signal (those not overlapped with nuclear Hoechst staining) were measured.

Immunoblot

Nuclear extracts were made from liver according to previously published protocol (*52*). Protein concentrations were determined by Bradford assays (Bio-Rad), and aliquots were snap-frozen in liquid nitrogen and stored at -80°C until usage. Immunoblot analyses were performed as described previously (*53*). Briefly, 25μg proteins separated by 4~20% gradient SDS-PAGE gels (Biorad) were transferred to nitrocellulose membranes, blocked in TBST buffer supplemented with 5% bovine serum albumin (BSA) or 5% fat-free milk and incubated overnight with primary anti-

SON antibody (abcam 121033), anti-BMAL1 antibody (abcam 3350), anti-PERK (Cell signaling, #3192), anti-phospho-PERK (Thr908) (Thermo Fisher, MA5-15033), anti-ATF4 (Cell signaling, #11815), anti-IRE1α (Cell signaling, #3294), anti-phospho-IRE1α (Ser724) (ABclonal, AP0878), anti-XBP1s (Biolegend, 658802), anti-ATF6 (Santa Cruz, sc-166659), β-ACTIN (Cell signaling, #12620) at 4°C. Blots were incubated with an appropriate secondary antibody coupled to horseradish peroxidase at room temperature for 1 hour, and reacted with ECL reagents per the manufacturer's (Thermo) suggestion and detected by Biorad ChemiDoc MP Imaging System.

qRT-PCR

Total mRNA was isolated from murine embryonic fibroblasts (MEFs) or mouse liver with PureLink RNA mini kit (Life Technologies) with additional on-column DNase digestion step to remove genomic DNA per the manufacturer's instructions. Reverse transcription was carried out using 5μg of RNA using Superscript III (Life Technologies) per the manufacturer's instructions. For gene expression analyses, cDNA samples were diluted 1/30-fold (for all other genes except for 18sRNA) and 1/900-fold (for 18sRNA). qPCR was performed using the SYBR green system with sequence-specific primers. All data were analyzed with 18S or *β-actin* as the endogenous control. qPCR primer sequences are as follows and all primers span introns, except for primers for quantifying pre-mRNAs:

Mouse total *Xbp1* forward primer: gggtctgctgagtcc
Mouse total *Xbp1* reverse primer: cagactcagaatctgaagagg
Mouse total *Xbp1* pre-mRNA forward primer: GTTAAGAACACGCTTGGGAATG
Mouse total *Xbp1* pre-mRNA reverse primer: TGGAGGTCCAGAACACAAAC
Mouse *Arntl* forward primer: gccccaccgacctactct
Mouse *Arntl* reverse primer: tgtctgtgtccatactttcttgg
Mouse *Per1* forward primer: tcctcctcctacactgcctct
Mouse *Per1* reverse primer: ttgctgacgacggatcttt
Mouse *Per2* forward primer: caacacagacgacagcatca
Mouse *Per2* reverse primer: tcctggtcctccttcaacac
Mouse *Cry2* forward primer: gcagagcctggttcaagc
Mouse *Cry2* reverse primer: gccactggatagtgctctgg
Mouse *Sec23b* forward primer: tgaccaaactggacttctgga
Mouse *Sec23b* reverse primer: aaagaatctcccatcaccatgt
Mouse *Son* forward primer: ttccgggaaatacaacagga
Mouse *Son* reverse primer: gggtggatttgtttcaccat
Mouse *Manf* forward primer: gacagccagatctgtgaactaaaa
Mouse *Manf* reverse primer: tttcacccggagcttcttc
Mouse *Manf* pre-mRNA forward primer: AGGGTATGCAGAGATGGTAGA
Mouse *Manf* pre-mRNA reverse primer: GATCTGTGAGAAGCTGAAGAAGA
Mouse *Hyou1* forward primer: GAGGCGAAACCCATTTTAGA
Mouse *Hyou1* reverse primer: GCTCTTCCTGTTCAGGTCCA
Mouse *Hyou1* pre-mRNA forward primer: ACCGCTACAGCCATGATTT
Mouse *Hyou1* pre-mRNA reverse primer: ATCATCTGGCAGGCACAC
Mouse *Atf4* forward primer: CCACTCCAGAGCATTCCTTTAG
Mouse *Atf4* reverse primer: CTCCTTTACACATGGAGGGATTAG
Mouse *Atf6* forward primer: CATGAAGTGGAAAGGACCAAATC
Mouse *Atf6* reverse primer: CAGCCATCAGCTGAGAATTAGA
Mouse *Ire1α* forward primer: TCCTAACAACCTGCCCAAAC

Mouse *Ire1α* reverse primer: TCTCCTCCACATCCTGAGATAC
Mouse 18s RNA forward primer: ctcaacacgggaaacctcac
Mouse 18s RNA reverse primer: cgctccaccaactaagaacg
Mouse *β-actin* forward primer: aaggccaaccgtgaaaagat
Mouse *β-actin* reverse primer: gtggtacgaccagaggcatac

Chromatin Immunoprecipitation (ChIP) and ChIP-Seq

ChIP for SC35 was performed using anti-SC35 antibody (ab11826, Abcam) as previously described (*53*). Briefly, mouse liver samples were submerged in PBS + 1% formaldehyde, cut into small (~1 mm3) pieces with a razor blade and incubated at room temperature for 15 minutes. Fixation was stopped by the addition of 0.125 M glycine (final concentration). The tissue pieces were then treated with a TissueTearer and finally spun down and washed twice in PBS. Chromatin was isolated by the addition of lysis buffer, followed by disruption with a Dounce homogenizer. The chromatin was enzymatically digested with MNase. Genomic DNA (Input) was prepared by treating aliquots of chromatin with RNase, Proteinase K and heated for reverse-crosslinking, followed by ethanol precipitation. Pellets were resuspended and the resulting DNA was quantified on a NanoDrop spectrophotometer. An aliquot of chromatin (10 µg) was precleared with protein A agarose beads (Invitrogen). Genomic DNA regions of interest were isolated using 4 µg of antibody. Complexes were washed, eluted from the beads with SDS buffer, and subjected to RNase and proteinase K treatment. Crosslinking was reversed by incubation overnight at 65 °C, and ChIP DNA was purified by phenol-chloroform extraction and ethanol precipitation. The DNA libraries were prepared at University of Pittsburgh and sequenced at Gene by Gene, Ltd per standard protocols. DNA libraries were prepared with Ovation® Ultralow V2 DNA-Seq library preparation kit (NuGen) using 1ng input DNA. The size selection for libraries were performed using SPRIselect beads (Beckman Coulter) and purity of the libraries were analyzed using the High Sensitivity DNA chip on Bioanalyzer 2100 (Agilent). The prepared libraries pooled and sequenced using Nova-Seq 6000 (Illumina), generating ~40 million 101 bp single-end reads per samples. ChIP-qPCR for MEFs were essentially performed the same way as previously described with anti-SC35 (ab11826, Abcam) and anti-XBP1s antibody (Biolegend 658802), except that the MEFs were directly fixed with 1% formaldehyde before subject to nuclei isolation and chromatin immunoprecipitation. The primers used for ChIP-qPCR are as follows:
Negative control region 1 forward primer: GCAACAACAACAGCAACAATAAC
Negative control region 1 reverse primer: CATGGCACCTAGAGTTGGATAA
Negative control region 2 forward primer: GCAGTATAACTTCTCACCCAAGT
Negative control region 2 reverse primer: AACATGGTGTCTGTTTGCTTTC
Xbp1 TSS region forward primer: GGCCACGACCCTAGAAAG
Xbp1 TSS region reverse primer: GGCTGGCCAGATAAGAGTAG
Xbp1 TTS region forward primer: CTTTCTCCACTCTCTGCTTCC
Xbp1 TTS region reverse primer: ACACTAGCAAGAAGATCCATCAA
Manf TSS region forward primer: ACAGCAGCAGCCAATGA
Manf TSS region reverse primer: CAGAAACCTGAGCTTCCCAT
Manf TTS region forward primer: CAACCTGCCACTAGATTGAAGA
Manf TTS region reverse primer: AGGCATCCTTGTGTGTCTATTT
Hyou1 TSS region forward primer: GACTTCGCAATCCACGAGAG
Hyou1 TSS region reverse primer: GACTTCTGCCAGCATCGG
Hyou1 gene body region forward primer: TGGAAGAGAAAGGTGGCTAAAG
Hyou1 gene body region reverse primer: TCCCAAGTGCTGGGATTAAAG

ChIP-Seq analysis

Replicates were pooled at each time for subsequent ChIP-Seq analysis. The sequences identified were mapped to the mouse genome (UCSC mm10) using BOWTIE function in Galaxy. Only the sequences uniquely mapped with no more than 2 mismatches were kept and used as valid reads. PCR duplicates were also removed. Peak calling was carried out by MACS2 (version 2.1.1.20160309) in Galaxy (options --mfold 5, 50 --pvalue 1e-4), on each ChIP-seq file against the input in $XBP1^{Flox}$ or $XBP1^{LKO}$ mice using the broad region function. To account for the different sequencing depths between samples, the signal files generated from MACS2 were RPKM normalized to sequencing depth (Meyer and Liu, 2014). 5,365 genes with at least one peak identified in the gene body region (from TSS to TTS) in at least one CT in $XBP1^{Flox}$ mice were identified.

RNA-Seq quantification

RNA-seq data was previous reported (*6*). Raw RNA-seq FASTQ files were analyzed by FastQC for quality control. Adaptors and low-quality reads were filtered by Trimmomatic (*54*). Then the processed reads were aligned by HISAT2 (*55*) against mouse reference mm10. For gene-level intron/exon quantification, bedtools software (*56*) was used to collect and count reads that aligned to any intron/exon of the given gene. If one read spans across multiple exons of the same gene, it will only be counted once. If one read spans intron/exon junction, it will only be counted as intron. The intron/exon count were normalized by gene length and total reads for FPKM normalization.

Estimation of mRNA processing rate

$$\text{Pre-mRNA } p(t) \xrightarrow{k_p(t)} \text{mature mRNA } m(t) \xrightarrow{k_d} \tag{3}$$

$$\frac{dm(t)}{dt} = k_p(t)p(t) - K_d m(t) \tag{4}$$

$$k_p(t) = \frac{\frac{dm(t)}{dt} + K_d m(t)}{p(t)} \tag{5}$$

The mRNA processing rate was estimated by the simple kinetic model (equation 3) where pre-mRNA [$p(t)$] was converted to mature mRNA [$m(t)$] with the mRNA processing rate k_p, which is also a function of time. We assume that the mature mRNA is subject to decay with a constant decay rate k_d. Therefore, the mRNA processing rate k_p (t) can be derived as equation 5. We utilized mRNA degradation rate for mouse genes reported in (*57*), and for gene without reported mRNA degradation rate, we used the mean value of 0.1 as a rough estimate. Since the original temporal gene expression data are fairly sparse (at 2h interval), in order to more accurately estimate the first derivative of mature mRNA [$m(t)/dt$], we performed a spline regression to obtain a more dense temporal dataset at 0.25h interval, and the first derivative at given time t is calculated as [$m(t+0.25)$-$m(t)$]/0.25. Data analysis was performed in Matlab and Excel.

Identification of oscillations from temporal dataset

Three orthogonal methods were used to identify oscillations from temporal dataset. Periodogram power spectral density was generated using Matlab with the pxx = periodogram (x) function.

Eigenvalue/pencil analysis was performed in Matlab with customarily written code as previously described (*4, 28*). Criterion for circadian genes are period between 21h to 25h, decay rate between 0.8 and 1.2; for ~12hr genes: period between 10.5h to 13.5h, decay rate between 0.8 and 1.2. The FDR rate was calculated with a permutation-based method as previously described (*6*). RAIN analysis was performed as previously described in Bioconductor (3.4) (http://www.bioconductor.org/packages/release/bioc/html/rain.html) (*17*). For temporal SC35 ChIP-Seq data in XBP1^{LKO} mice, a polynomial detrend (n=2) was first applied before subject to oscillation-identification algorithms. For all time lapse microscopy data, the raw data, rather than the spline regression fit, was used to identify oscillations.

REFERENCES AND NOTES:

1. B. Zhu, C. C. Dacso, B. W. O'Malley, Unveiling "Musica Universalis" of the Cell: A Brief History of Biological 12-Hour Rhythms. *J Endocr Soc* **2**, 727-752 (2018).
2. M. E. Hughes, L. DiTacchio, K. R. Hayes, C. Vollmers, S. Pulivarthy, J. E. Baggs, S. Panda, J. B. Hogenesch, Harmonics of circadian gene transcription in mammals. *PLoS Genet* **5**, e1000442 (2009).
3. G. Cretenet, M. Le Clech, F. Gachon, Circadian clock-coordinated 12 Hr period rhythmic activation of the IRE1alpha pathway controls lipid metabolism in mouse liver. *Cell Metab* **11**, 47-57 (2010).
4. B. Zhu, Q. Zhang, Y. Pan, E. M. Mace, B. York, A. C. Antoulas, C. C. Dacso, B. W. O'Malley, A Cell-Autonomous Mammalian 12 hr Clock Coordinates Metabolic and Stress Rhythms. *Cell Metab* **25**, 1305-1319 e1309 (2017).
5. H. Meng, N. M. Gonzales, D. M. Lonard, N. Putluri, B. Zhu, C. C. Dacso, B. York, B. W. O'Malley, XBP1 links the 12-hour clock to NAFLD and regulation of membrane fluidity and lipid homeostasis. *Nature Communications* **11**, 6215 (2020).
6. Y. Pan, H. Ballance, H. Meng, N. Gonzalez, S.-M. Kim, L. Abdurehman, B. York, X. Chen, Y. Schnytzer, O. Levy, C. C. Dacso, C. A. McClung, B. W. O'Malley, S. Liu, B. Zhu, 12-h clock regulation of genetic information flow by XBP1s. *PLOS Biology* **18**, e3000580 (2020).
7. B. Zhu, Decoding the function and regulation of the mammalian 12h-clock. *Journal of Molecular Cell Biology*, (2020).
8. R. Sriburi, S. Jackowski, K. Mori, J. W. Brewer, XBP1: a link between the unfolded protein response, lipid biosynthesis, and biogenesis of the endoplasmic reticulum. *J Cell Biol* **167**, 35-41 (2004).
9. Y. Wang, L. Song, M. Liu, R. Ge, Q. Zhou, W. Liu, R. Li, J. Qie, B. Zhen, Y. Wang, F. He, J. Qin, C. Ding, A proteomics landscape of circadian clock in mouse liver. *Nat Commun* **9**, 1553 (2018).
10. J. Wang, D. Mauvoisin, E. Martin, F. Atger, A. N. Galindo, L. Dayon, F. Sizzano, A. Palini, M. Kussmann, P. Waridel, M. Quadroni, V. Dulic, F. Naef, F. Gachon, Nuclear Proteomics Uncovers Diurnal Regulatory Landscapes in Mouse Liver. *Cell Metab* **25**, 102-117 (2017).
11. N. Saitoh, C. S. Spahr, S. D. Patterson, P. Bubulya, A. F. Neuwald, D. L. Spector, Proteomic analysis of interchromatin granule clusters. *Mol Biol Cell* **15**, 3876-3890 (2004).
12. D. L. Spector, A. I. Lamond, Nuclear speckles. *Cold Spring Harb Perspect Biol* **3**, (2011).
13. J. Fei, M. Jadaliha, T. S. Harmon, I. T. S. Li, B. Hua, Q. Hao, A. S. Holehouse, M. Reyer, Q. Sun, S. M. Freier, R. V. Pappu, K. V. Prasanth, T. Ha, Quantitative analysis of multilayer organization of proteins and RNA in nuclear speckles at super resolution. *J Cell Sci* **130**, 4180-4192 (2017).
14. Y. Shin, Y. C. Chang, D. S. W. Lee, J. Berry, D. W. Sanders, P. Ronceray, N. S. Wingreen, M. Haataja, C. P. Brangwynne, Liquid Nuclear Condensates Mechanically Sense and Restructure the Genome. *Cell* **176**, 1518 (2019).

15. D. Bracha, M. T. Walls, M. T. Wei, L. Zhu, M. Kurian, J. L. Avalos, J. E. Toettcher, C. P. Brangwynne, Mapping Local and Global Liquid Phase Behavior in Living Cells Using Photo-Oligomerizable Seeds. *Cell* **175**, 1467-1480 e1413 (2018).
16. J. Kim, K. Y. Han, N. Khanna, T. Ha, A. S. Belmont, Nuclear speckle fusion via long-range directional motion regulates speckle morphology after transcriptional inhibition. *J Cell Sci* **132**, (2019).
17. P. F. Thaben, P. O. Westermark, Detecting rhythms in time series with RAIN. *J Biol Rhythms* **29**, 391-400 (2014).
18. P. Bhat, D. Honson, M. Guttman, Nuclear compartmentalization as a mechanism of quantitative control of gene expression. *Nat Rev Mol Cell Biol* **22**, 653-670 (2021).
19. A. Sharma, H. Takata, K. Shibahara, A. Bubulya, P. A. Bubulya, Son is essential for nuclear speckle organization and cell cycle progression. *Mol Biol Cell* **21**, 650-663 (2010).
20. A. Atwood, R. DeConde, S. S. Wang, T. C. Mockler, J. S. Sabir, T. Ideker, S. A. Kay, Cell-autonomous circadian clock of hepatocytes drives rhythms in transcription and polyamine synthesis. *Proc Natl Acad Sci U S A* **108**, 18560-18565 (2011).
21. F. Rijo-Ferreira, J. S. Takahashi, Genomics of circadian rhythms in health and disease. *Genome Med* **11**, 82 (2019).
22. H. Ballance, B. Zhu, Revealing the hidden reality of the mammalian 12-h ultradian rhythms. *Cellular and Molecular Life Sciences*, (2021).
23. M. Sorek, Y. Schnytzer, H. W. Ben-Asher, V. C. Caspi, C. S. Chen, D. J. Miller, O. Levy, Setting the pace: host rhythmic behaviour and gene expression patterns in the facultatively symbiotic cnidarian Aiptasia are determined largely by Symbiodinium. *Microbiome* **6**, 83 (2018).
24. Y. Schnytzer, N. Simon-Blecher, J. Li, H. W. Ben-Asher, M. Salmon-Divon, Y. Achituv, M. E. Hughes, O. Levy, Tidal and diel orchestration of behaviour and gene expression in an intertidal mollusc. *Scientific Reports* **8**, 4917 (2018).
25. A. Chavez, M. Tuttle, B. W. Pruitt, B. Ewen-Campen, R. Chari, D. Ter-Ovanesyan, S. J. Haque, R. J. Cecchi, E. J. K. Kowal, J. Buchthal, B. E. Housden, N. Perrimon, J. J. Collins, G. Church, Comparison of Cas9 activators in multiple species. *Nat Methods* **13**, 563-567 (2016).
26. Y. E. Guo, J. C. Manteiga, J. E. Henninger, B. R. Sabari, A. Dall'Agnese, N. M. Hannett, J. H. Spille, L. K. Afeyan, A. V. Zamudio, K. Shrinivas, B. J. Abraham, A. Boija, T. M. Decker, J. K. Rimel, C. B. Fant, T. I. Lee, Cisse, II, P. A. Sharp, D. J. Taatjes, R. A. Young, Pol II phosphorylation regulates a switch between transcriptional and splicing condensates. *Nature* **572**, 543-548 (2019).
27. J. A. West, C. P. Davis, H. Sunwoo, M. D. Simon, R. I. Sadreyev, P. I. Wang, M. Y. Tolstorukov, R. E. Kingston, The long noncoding RNAs NEAT1 and MALAT1 bind active chromatin sites. *Mol Cell* **55**, 791-802 (2014).
28. A. C. Antoulas, B. Zhu, Q. Zhang, B. York, B. W. O'Malley, C. C. Dacso, A novel mathematical method for disclosing oscillations in gene transcription: A comparative study. *PLoS One* **13**, e0198503 (2018).
29. J. Kim, N. Khanna, A. S. Belmont, Transcription amplification by nuclear speckle association. *bioRxiv*, 604298 (2019).
30. J. Wang, L. Symul, J. Yeung, C. Gobet, J. Sobel, S. Luck, P. O. Westermark, N. Molina, F. Naef, Circadian clock-dependent and -independent posttranscriptional regulation underlies temporal mRNA accumulation in mouse liver. *Proc Natl Acad Sci U S A* **115**, E1916-E1925 (2018).
31. P. Walter, D. Ron, The unfolded protein response: from stress pathway to homeostatic regulation. *Science* **334**, 1081-1086 (2011).

32. J. Yu, T. Li, Y. Liu, X. Wang, J. Zhang, X. Wang, G. Shi, J. Lou, L. Wang, C. C. Wang, L. Wang, Phosphorylation switches protein disulfide isomerase activity to maintain proteostasis and attenuate ER stress. *EMBO J* **39**, e103841 (2020).
33. Y. Liu, M. Fares, N. P. Dunham, Z. Gao, K. Miao, X. Jiang, S. S. Bollinger, A. K. Boal, X. Zhang, AgHalo: A Facile Fluorogenic Sensor to Detect Drug-Induced Proteome Stress. *Angew Chem Int Ed Engl* **56**, 8672-8676 (2017).
34. N. Schaum, B. Lehallier, O. Hahn, S. Hosseinzadeh, S. E. Lee, R. Sit, D. P. Lee, P. M. Losada, M. E. Zardeneta, R. Pálovics, T. Fehlmann, J. Webber, A. McGeever, H. Zhang, D. Berdnik, W. Tan, A. Zee, M. Tan, A. Pisco, J. Karkanias, N. F. Neff, A. Keller, S. Darmanis, S. R. Quake, T. Wyss-Coray, The murine transcriptome reveals global aging nodes with organ-specific phase and amplitude. *bioRxiv*, 662254 (2019).
35. M. Geyfman, V. Kumar, Q. Liu, R. Ruiz, W. Gordon, F. Espitia, E. Cam, S. E. Millar, P. Smyth, A. Ihler, J. S. Takahashi, B. Andersen, Brain and muscle Arnt-like protein-1 (BMAL1) controls circadian cell proliferation and susceptibility to UVB-induced DNA damage in the epidermis. *Proc Natl Acad Sci U S A* **109**, 11758-11763 (2012).
36. R. Zhang, N. F. Lahens, H. I. Ballance, M. E. Hughes, J. B. Hogenesch, A circadian gene expression atlas in mammals: implications for biology and medicine. *Proc Natl Acad Sci U S A* **111**, 16219-16224 (2014).
37. M. Perelis, B. Marcheva, K. Moynihan Ramsey, M. J. Schipma, A. L. Hutchison, A. Taguchi, C. B. Peek, H. Hong, W. Huang, C. Omura, A. L. Allred, C. A. Bradfield, A. R. Dinner, G. D. Barish, J. Bass, Pancreatic β cell enhancers regulate rhythmic transcription of genes controlling insulin secretion. *Science* **350**, aac4250 (2015).
38. A. S. Lyon, W. B. Peeples, M. K. Rosen, A framework for understanding the functions of biomolecular condensates across scales. *Nat Rev Mol Cell Biol* **22**, 215-235 (2021).
39. M. Mofatteh, F. Echegaray-Iturra, A. Alamban, F. Dalla Ricca, A. Bakshi, M. G. Aydogan, Autonomous clocks that regulate organelle biogenesis, cytoskeletal organization, and intracellular dynamics. *eLife* **10**, e72104 (2021).
40. D. S. W. Lee, N. S. Wingreen, C. P. Brangwynne, Chromatin mechanics dictates subdiffusion and coarsening dynamics of embedded condensates. *Nature Physics* **17**, 531-538 (2021).
41. A. W. Folkmann, A. Putnam, C. F. Lee, G. Seydoux, Regulation of biomolecular condensates by interfacial protein clusters. *Science* **373**, 1218-1224 (2021).
42. S. E. Hasenson, Y. Shav-Tal, Speculating on the Roles of Nuclear Speckles: How RNA-Protein Nuclear Assemblies Affect Gene Expression. *Bioessays* **42**, e2000104 (2020).
43. K. A. Alexander, A. Cote, S. C. Nguyen, L. Zhang, O. Gholamalamdari, P. Agudelo-Garcia, E. Lin-Shiao, K. M. A. Tanim, J. Lim, N. Biddle, M. C. Dunagin, C. R. Good, M. R. Mendoza, S. C. Little, A. Belmont, E. F. Joyce, A. Raj, S. L. Berger, p53 mediates target gene association with nuclear speckles for amplified RNA expression. *Mol Cell* **81**, 1666-1681 e1666 (2021).
44. D. Gems, L. Partridge, Stress-response hormesis and aging: "that which does not kill us makes us stronger". *Cell Metab* **7**, 200-203 (2008).
45. A. H. Lee, E. F. Scapa, D. E. Cohen, L. H. Glimcher, Regulation of hepatic lipogenesis by the transcription factor XBP1. *Science* **320**, 1492-1496 (2008).
46. O. Shalem, N. E. Sanjana, E. Hartenian, X. Shi, D. A. Scott, T. Mikkelson, D. Heckl, B. L. Ebert, D. E. Root, J. G. Doench, F. Zhang, Genome-scale CRISPR-Cas9 knockout screening in human cells. *Science* **343**, 84-87 (2014).
47. A. Chavez, J. Scheiman, S. Vora, B. W. Pruitt, M. Tuttle, P. R. I. E, S. Lin, S. Kiani, C. D. Guzman, D. J. Wiegand, D. Ter-Ovanesyan, J. L. Braff, N. Davidsohn, B. E. Housden, N. Perrimon, R. Weiss, J. Aach, J. J. Collins, G. M. Church, Highly efficient Cas9-mediated transcriptional programming. *Nat Methods* **12**, 326-328 (2015).

48. E. Stashi, R. B. Lanz, J. Mao, G. Michailidis, B. Zhu, N. M. Kettner, N. Putluri, E. L. Reineke, L. C. Reineke, S. Dasgupta, A. Dean, C. R. Stevenson, N. Sivasubramanian, A. Sreekumar, F. Demayo, B. York, L. Fu, B. W. O'Malley, SRC-2 is an essential coactivator for orchestrating metabolism and circadian rhythm. *Cell Rep* **6**, 633-645 (2014).
49. T. Sakuma, S. Nakade, Y. Sakane, K.-I. T. Suzuki, T. Yamamoto, MMEJ-assisted gene knock-in using TALENs and CRISPR-Cas9 with the PITCh systems. *Nature Protocols* **11**, 118-133 (2016).
50. B. Zhu, C. Khozoie, M. T. Bility, C. H. Ferry, N. Blazanin, A. B. Glick, F. J. Gonzalez, J. M. Peters, Peroxisome proliferator-activated receptor beta/delta cross talks with E2F and attenuates mitosis in HRAS-expressing cells. *Mol Cell Biol* **32**, 2065-2082 (2012).
51. G. Koulouras, A. Panagopoulos, M. A. Rapsomaniki, N. N. Giakoumakis, S. Taraviras, Z. Lygerou, EasyFRAP-web: a web-based tool for the analysis of fluorescence recovery after photobleaching data. *Nucleic Acids Res* **46**, W467-W472 (2018).
52. A. Malovannaya, R. B. Lanz, S. Y. Jung, Y. Bulynko, N. T. Le, D. W. Chan, C. Ding, Y. Shi, N. Yucer, G. Krenciute, B. J. Kim, C. Li, R. Chen, W. Li, Y. Wang, B. W. O'Malley, J. Qin, Analysis of the human endogenous coregulator complexome. *Cell* **145**, 787-799 (2011).
53. B. Zhu, L. A. Gates, E. Stashi, S. Dasgupta, N. Gonzales, A. Dean, C. C. Dacso, B. York, B. W. O'Malley, Coactivator-Dependent Oscillation of Chromatin Accessibility Dictates Circadian Gene Amplitude via REV-ERB Loading. *Mol Cell* **60**, 769-783 (2015).
54. A. M. Bolger, M. Lohse, B. Usadel, Trimmomatic: a flexible trimmer for Illumina sequence data. *Bioinformatics* **30**, 2114-2120 (2014).
55. D. Kim, B. Langmead, S. L. Salzberg, HISAT: a fast spliced aligner with low memory requirements. *Nat Methods* **12**, 357-360 (2015).
56. A. R. Quinlan, I. M. Hall, BEDTools: a flexible suite of utilities for comparing genomic features. *Bioinformatics* **26**, 841-842 (2010).
57. L. V. Sharova, A. A. Sharov, T. Nedorezov, Y. Piao, N. Shaik, M. S. Ko, Database for mRNA half-life of 19 977 genes obtained by DNA microarray analysis of pluripotent and differentiating mouse embryonic stem cells. *DNA Res* **16**, 45-58 (2009).
58. H. Yoshida, M. Oku, M. Suzuki, K. Mori, pXBP1(U) encoded in XBP1 pre-mRNA negatively regulates unfolded protein response activator pXBP1(S) in mammalian ER stress response. *J Cell Biol* **172**, 565-575 (2006).
59. H. Li, A. V. Korennykh, S. L. Behrman, P. Walter, Mammalian endoplasmic reticulum stress sensor IRE1 signals by dynamic clustering. *Proc Natl Acad Sci U S A* **107**, 16113-16118 (2010).
60. J. B. DuRose, A. B. Tam, M. Niwa, Intrinsic capacities of molecular sensors of the unfolded protein response to sense alternate forms of endoplasmic reticulum stress. *Mol Biol Cell* **17**, 3095-3107 (2006).

Acknowledgments:

We want to thank Dr. Toren Finkel for sharing us with the lentiCRISPRv2 plasmid, as well as valuable input and discussion during the manuscript preparation. We further want to thank Leymaan Abdurehman and Haiyue Li for technical support on immunofluorescence and qPCR.

Funding:

National Institute of Health grant DP2GM140924 (BZ)
National Institute of Health grant T32AG021885 (HB)
American Diabetes Association grant 1-18-JDF-025 (BZ)
National Institute of Health grant P30DK120531 (BZ, SL)

EW Biomedical Scholars Program 00033066 (XZ)
National Science Foundation grant CHE-1944973 (XZ)

Author contributions:

Conceptualization: BZ

Methodology: BZ, HB, XZ

Investigation: BZ, HB, WD, SI, CE, YP, JZ, MS and JL.

Visualization: BZ, WD.

Formal Analysis: BZ, WD, JL, SL.

Funding acquisition: BZ and XZ.

Resources: BZ

Software: BZ

Validation: BZ, WD, HB.

Supervision: BZ

Writing – original draft: BZ

Writing – review & editing: all authors

Competing interests:

The authors declare no competing interests.

Data and materials availability:

All raw and processed sequencing data generated in this study have been submitted to the NCBI Gene Expression Omnibus (GEO; http://www.ncbi.nlm.nih.gov/geo/) under accession numbers GSE174170. All data needed to evaluate the conclusions in the paper are present in the paper and/or the Supplementary Materials.

Figure legends:

Fig. 1. XBP1s regulates a cell-autonomous 12h rhythm of nuclear speckle morphology change. (**A**) 3D reconstruction of immunofluorescence of SC35 co-stained with DAPI in the liver of XBP1^{Flox} and XBP1^{LKO} mice at different CT. **(B)** Cartoon showing the different nuclear speckle LLPS patterns at different CT in XBP1^{Flox} mice (top) and violin plot quantification of weighted sphericity of nuclear speckles in XBP1^{Flox} and XBP1^{LKO} mice liver at different CT. n=150~400 nuclei from 3 mice per CT. P values of exhibiting statistically significant 12h rhythms by RAIN analysis in XBP1^{Flox} and XBP1^{LKO} mice were also shown. (**C-E**) GFP::SC35 MEFs were serum synchronized and subject to time lapse imaging. Selective images and quantification of temporal sphericity from one single GFP::SC35 MEF. Narrow line: raw data, thick line: spline fit (**C**). Temporal sphericity (6 to 10 cells quantified at any given time; gray area: mean ± SEM; solid line: spline fit) and period distribution of dominant sphericity rhythms in single cells quantified by the eigenvalue/pencil method (n=25) (**D**). Temporal sphericity of GFP::SC35 MEFs expressing control, *Bmal1* or *Xbp1* sgRNA (6 to 10 cells quantified at any given time; light area: mean ± SEM; solid line: spline fit), and periodogram analysis of average sphericity rhythms in the three groups (**E**). Gray areas in D and E indicates two hours of serum shock.

Fig. 2. An evolutionarily conserved XBP1s-SON axis controls 12h rhythm of cell-autonomous nuclear speckle LLPS dynamics. (**A, B**) Representative Western blot (**A**) and quantification (**B**) (n=2~4) of hepatic nuclear SON protein (normalized to the Ponceau S staining intensity), superimposed with the average nuclear speckle sphericity and morphology cartoons at different CT. The same CT32 sample was run twice to enable comparison across different gels. (**C**) qPCR analysis of hepatic *Son* in in the liver of XBP1^{Flox} and XBP1^{LKO} mice at different CT. Periods calculated by the eigenvalue/pencil method were also shown. (**D, E**) RNA-seq data of *Son* orthologs expression in *A. diaphaha* (**D**) and *C. rota* (**E**). (**F, G**) Immunofluorescence of SC35 co-stained with DAPI in scrambled or *Son* siRNA MEFs (**F**) and quantification of sphericity (n=40~100) (**G**). (**H-J**) GFP::SC35 MEFs were transfected with non-targeting scrambled or *Son* siRNA. Temporal sphericity (5 to 10 cells quantified at any given time; light area: mean ± SEM; solid line: spline fit), and calculated periods by the eigenvalue/pencil method after serum synchronization (**H**). FRAP analysis with representative recovery curve (**I**) (data showing quantification from 3 speckles per cell; mean ± SEM for each point; solid line: spline fit) and quantified recovery half-life (**J**). (**K**) Calculated temporal sphericity and recovery half-life of nuclear speckles from serum synchronized GFP::SC35 MEFs. n=7 to 10 cells for FRAP analysis; Sphericity was calculated from the average sphericity of each image (n=6) with ~20 nuclear speckles on each image that are captured before photo-bleaching. Dash line: raw data; solid line: spline fit.

Fig. 3. XBP1s regulates 12h rhythmic nuclear speckle-chromatin interactions. (**A**) Heat map of temporal SC35 ChIP-seq signal as well as input signal for 5,365 genes in XBP1^{Flox} and XBP1^{LKO} mice from 10kb upstream of transcription start site (TSS) to 10kb downstream of transcription termination site (TTS) for each gene. (**B**) GO analysis of all 5,365 genes or 3,207 genes with strong SC35 ChIP signal. (**C**) Illustration on the workflow to estimate the pre-mRNA and mature-mRNA level, as well the as the mRNA processing rate from temporal RNA-Seq data. (**D**) Heat maps of relative integrated SC35 binding signal over gene bodies, pre-mRNA and mature mRNA expression, and estimated mRNA processing rate (with amplitude for 12h rhythm) at different CT in XBP1^{Flox} and XBP1^{LKO} mice. (**E**) Polar histogram demonstrating the phase distributions of 12h rhythmic mRNA processing rates for genes with (top) or without (bottom) strong SC35 signal in

XBP1^{Flox} mice. (**F**) Log_2 transformed amplitude of 12h mRNA processing rates for genes with or without strong SC35 binding in XBP1^{Flox} and XBP1^{LKO} mice. (**G**) Scatter plot of the amplitude of log_2 transformed 12h mRNA processing rates versus integrated 12h SC35 binding signal over gene bodies for 1,160 genes having both in XBP1^{Flox} mice. (**H**) Period distribution of pre and mature-mRNA oscillations for 1,160 genes in G. (**I-K**) Temporal expression of *Rela* at the pre-mRNA (**I**), mature mRNA (**J**) level in XBP1^{Flox} and XBP1^{LKO} mice, and integrated SC35 gene body signal and mRNA processing rate in XBP1^{Flox} mice (**K**). Data: Mean ±SEM in I and J.

Fig. 4. Proteostasis gene expressions are hyper-sensitive to nuclear speckle LLPS dynamic change. (**A**) Scatter plot demonstrating the phases of 12h rhythm of nuclear speckle-chromatin interactions (x axis) versus those of 12h rhythm of pre-mRNA expression (y axis) for 528 genes. Two major clusters of genes are highlighted in red and blue, respectively. (**B**) GO analysis of 130 genes highlighted in red and 260 genes highlighted in blue. (**C**) Quantification of the phases of 12h rhythms of nuclear speckle-chromatin interaction, XBP1s chromatin binding, pre and mature mRNA expression of 69 genes that exhibit all four, with temporal profile for *Xbp1* gene also shown. Data: Mean ±SEM (**D**) A simplified model demonstrating that SON can positively regulate nuclear speckles fluidity and their interactions with chromatin, and subsequent gene expression involved in proteostasis and UPR.

Fig. 5. Temporal kinetics of UPR in response to low level of ER stress recapitulates endogenous 12h oscillator. MEFs were treated with 100ng/ml of Tu for different hours. (**A**) FRAP assay and quantification of nuclear speckle sphericity. (**B**) Western blot and quantification (normalized to total Ponceau S staining intensity) of SON and XBP1s expression. (**C**) qPCR analysis of pre-mRNA level of different UPR genes. (**D**) Selected genes aligned for SC35 and XBP1s ChIP-seq signal from CT12 in XBP1^{Flox} mice (left) and ChIP-qPCR of XBP1s and SC35 on selected regions (indicated by red bars) (right). Data: Mean ± SEM.

Fig. 6. SON is required for co-localization of nuclear speckles with XBP1s during ER stress. MEFs were transfected with control or *Son* siRNAs and treated with 100ng/ml Tu for 6h. (**A**) ChIP-qPCR of SC35 on transcription start site (TSS) and transcription termination sites (TES) of gene bodies of selective UPR genes. Data: Mean ± SEM. (**B**) Immunofluorescence of anti-XBP1s (red), GFP signal (green) from GFP::SC35 fusion protein and DAPI nuclei staining (blue) as well as merged images of either two or all three channels. Representative images (**left**), Manders' coefficient quantification of co-localization of SC35/XBP1s and SC35/chromatin signals (**top right**), and quantification of log_2 transformed ratio of nuclear to cytosol level of XBP1s (**bottom right**). Box and whiskers plot showing minimum to maximum values.

Fig. 7. SON amplifies the UPR transcriptionally. (**A**) MEFs were transiently transfected with scramble control or *Son* siRNA and treated with 100ng/ml of Tu for 6 hours and qPCR analysis were performed on selective genes. (**B**) Control MEFs or MEFs with dCAS9-VPR-mediated stable overexpression of *Son* were treated with 100ng/ml of Tu for 6 hours and qPCR analysis were performed on selective genes. (**C-E**) MEFs were transiently transfected with scramble control or *Son* siRNA and treated with 100ng/ml of Tu for 6 hours and qPCR analysis (**C**) and representative western blot images (**D**) and quantification (**E**). (**F-H**) Control MEFs or MEFs with dCAS9-VPR-mediated stable overexpression of *Son* were treated with 100ng/ml of Tu for 6 hours and qPCR analysis (**F**) and representative western blot images (**G**) and quantification (**H**). For p-IRE1α, DMSO condition expression is too low to be accurately quantified. Data: Mean ± SEM.

Fig. 8. SON protects cells against proteome stress. (**A-C**) MEFs were transiently transfected with $AgHalo_{ER}$ plasmid and then further transfected with control or *Son* siRNAs and treated with different concentrations of Tu for 16h before subject to confocal live imaging. Representative confocal images of DAPI staining and $AgHalo_{ER}$-probe conjugates in response to Tu (**C**). Quantification of averaged AgHalo-probe intensity per cell (**D**) and averaged cell number per area of 35000 μm^2 (**E**). Each data point in B is averaged intensity per cell calculated from each image of 35000 μm^2 area. (**D-F**) dCAS9-VPR GFP::SC35 MEFs expressing control or *Son* promoter-targeting sgRNA were transiently transfected with $AgHalo_{ER}$ plasmid and then treated with 100ng/ml tunicamycin (Tu) for 16h before subject to confocal live imaging. Representative confocal images of DAPI staining and ER-targeting $AgHalo_{ER}$-probe conjugates in response to 100ng/ml Tu (**D**). White arrows indicate ER-targeting $AgHalo_{ER}$-probe conjugates. Quantification of averaged AgHalo-probe intensity (non-nuclear portion) per cell (**E**) and averaged cell number per area of 35000 μm^2 (**F**). Each data point in E is averaged intensity per cell calculated from each image of 35000 μm^2 area. Data: Mean ± SEM.

Fig. 9. Correlative hepatic *Son* and UPR gene expression dynamics is observed across the mouse life span. Expression of *Son* and UPR genes in a 28h time window (**A**) or across the entire mouse life span (**B**) in mouse liver. Solid line: mean; shaded area: 95% confidence interval.

Fig. 10. XBP1s-SON axis spatiotemporally controls nuclear speckle LLPS to regulate proteostasis. An analogy would be the water level fluctuations in a lake: Nuclear speckles with higher SON level is like a lake filled with free-flowing water with fast dynamics, while nuclear speckles with reduced SON expression resemble a nearly dried-out lake with a few disconnected pools of stagnant water. Our study further indicates that the nuclear speckle LLPS may be a novel therapeutic target for pathologies that arise as a result of dysregulated proteostasis. Please refer to discussion section for details.

Science Advances
AAAS

Supplementary Materials for

Four-dimensional nuclear speckle phase separation dynamics regulate proteostasis

William Dion[1†], Heather Ballance[1†], Jane Lee[1], Yinghong Pan[2], Saad Irfan[1], Casey Edwards[1], Michelle Sun[1], Jing Zhang[1], Xin Zhang[3], Silvia Liu[4,5], Bokai Zhu[1,4,6] *

* Correspondence author. Email: bzhu@pitt.edu (B.Z.)

This PDF file includes:

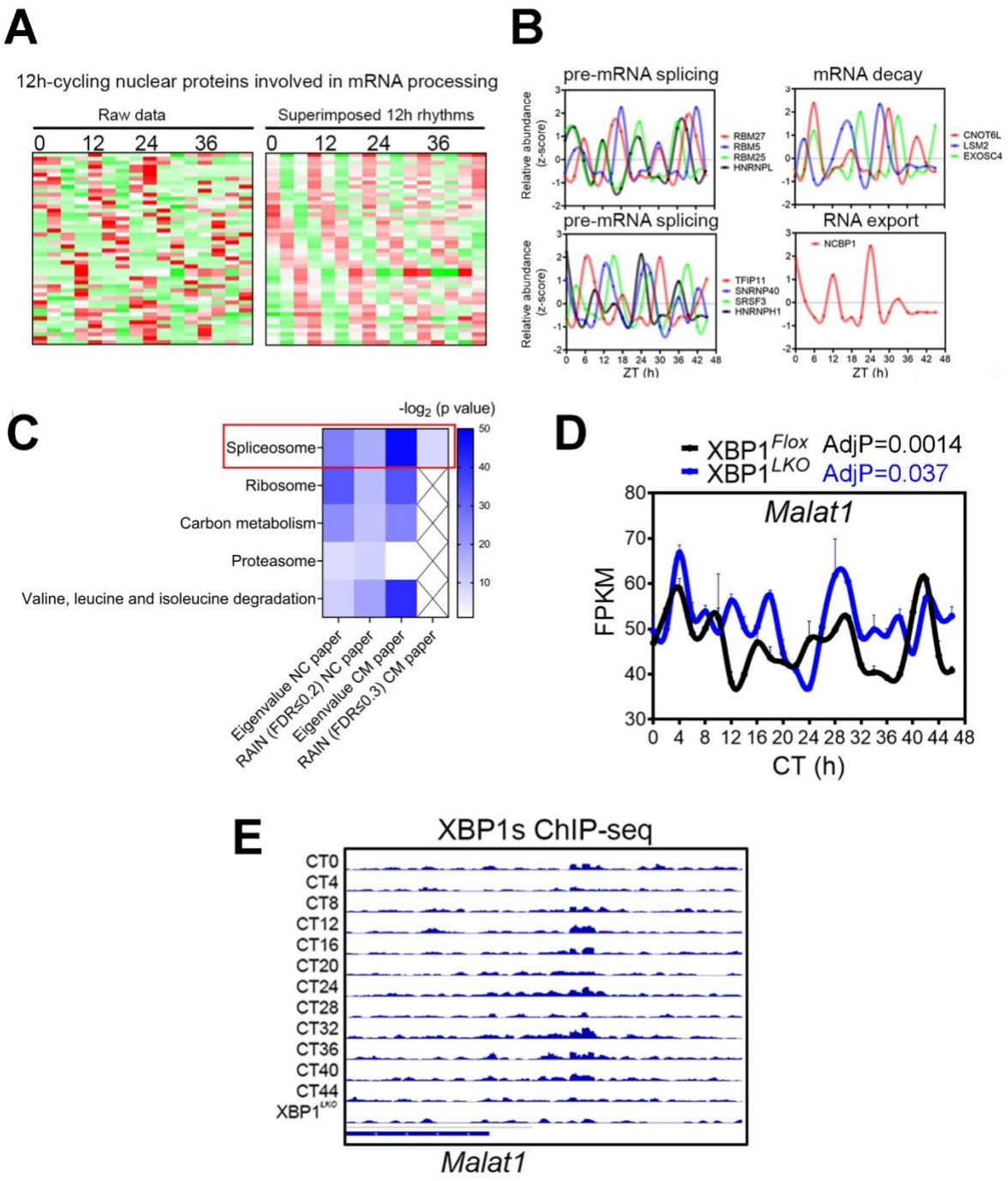

fig. S1. 12h rhythm of mRNA processing protein expression is prevalent in mouse liver. (**A**) Heat map of raw and superimposed 12h rhythms of nuclear proteins involved in mRNA metabolism as originally reported in (*9*). (**B**) Relative abundance of representative proteins at different zeitgeber time (ZT) as originally reported in (*9*). (**C**) GO analysis of 12h nuclear proteins reported in the *Nature Communications* (NC) (*9*) and *Cell Metabolism* (CM) (*10*) studies that are identified by either the eigenvalue/pencil or the RAIN method. (**D**) RNA-Seq data of *Malat1* expression in XBP1^{Flox} and XBP1^{LKO} mice (*Malat1* is intronless) with FDR adjusted p values by RAIN analysis shown. Data: Mean ± SEM. (**E**) Snapshot of XBP1s ChIP-Seq on *Malat1* promoter.

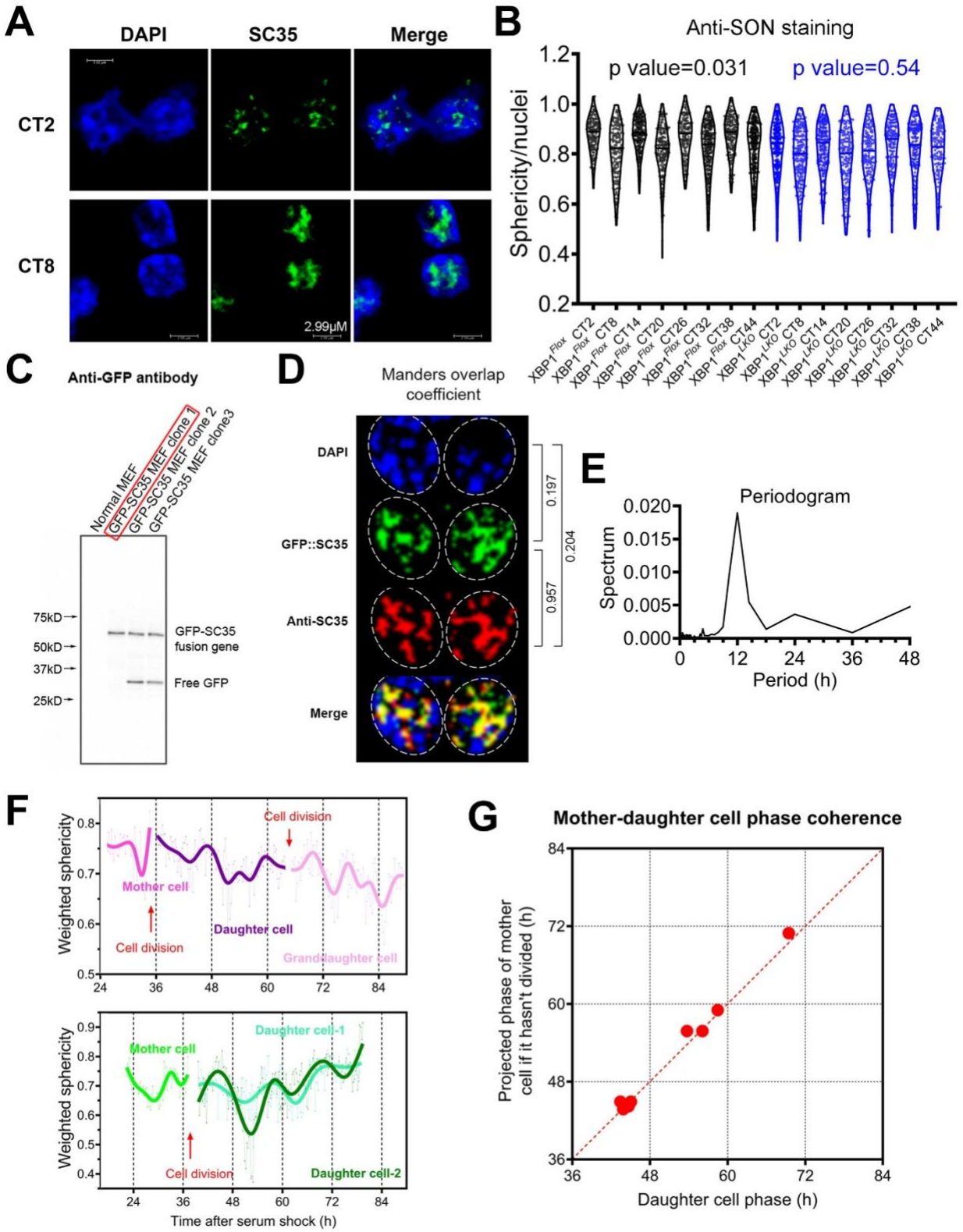

fig. S2. 12h rhythm of nuclear speckle morphology change is separate from the cell cycle. (**A**) Confocal immunofluorescence against SC35 co-stained with DAPI in the liver of XBP1^{Flox} at different CT. (**B**) Violin plot quantification of weighted sphericity of nuclear speckles in XBP1^{Flox}

and XBP1^{LKO} mice liver at different CT based upon anti-SON immunofluorescence signal. n=130~300 nuclei from 3 mice per CT. P values of exhibiting statistically significant 12h rhythms by RAIN analysis in XBP1^{Flox} and XBP1^{LKO} mice were also shown. (**C**) Anti-GFP western blot of normal as well three monoclonal lines of GFP::SC35 MEFs. Clone 1 is used in this study. (**D**) Confocal immunofluorescence against SC35 overlapped with GFP signal and co-stained with DAPI in GFP::SC35 MEFs. Manders coefficient between different signal are also shown. (**E**) Periodogram demonstrating cell-autonomous dominant 12h rhythmic nuclear speckle morphology change in MEFs, calculated from the raw average sphericity data in Fig. 1D. (**F**) Quantification of temporal sphericity from single GFP::SC35 MEFs at different times post serum synchronization. After each cell division, the temporal sphericity of daughter cells are continuously plotted after the mother cell. Narrow line: raw data, thick line: spline fit. (**G**) Scatter plot showing the phase relationship between the daughter cell and the mother cell if it hadn't divided.

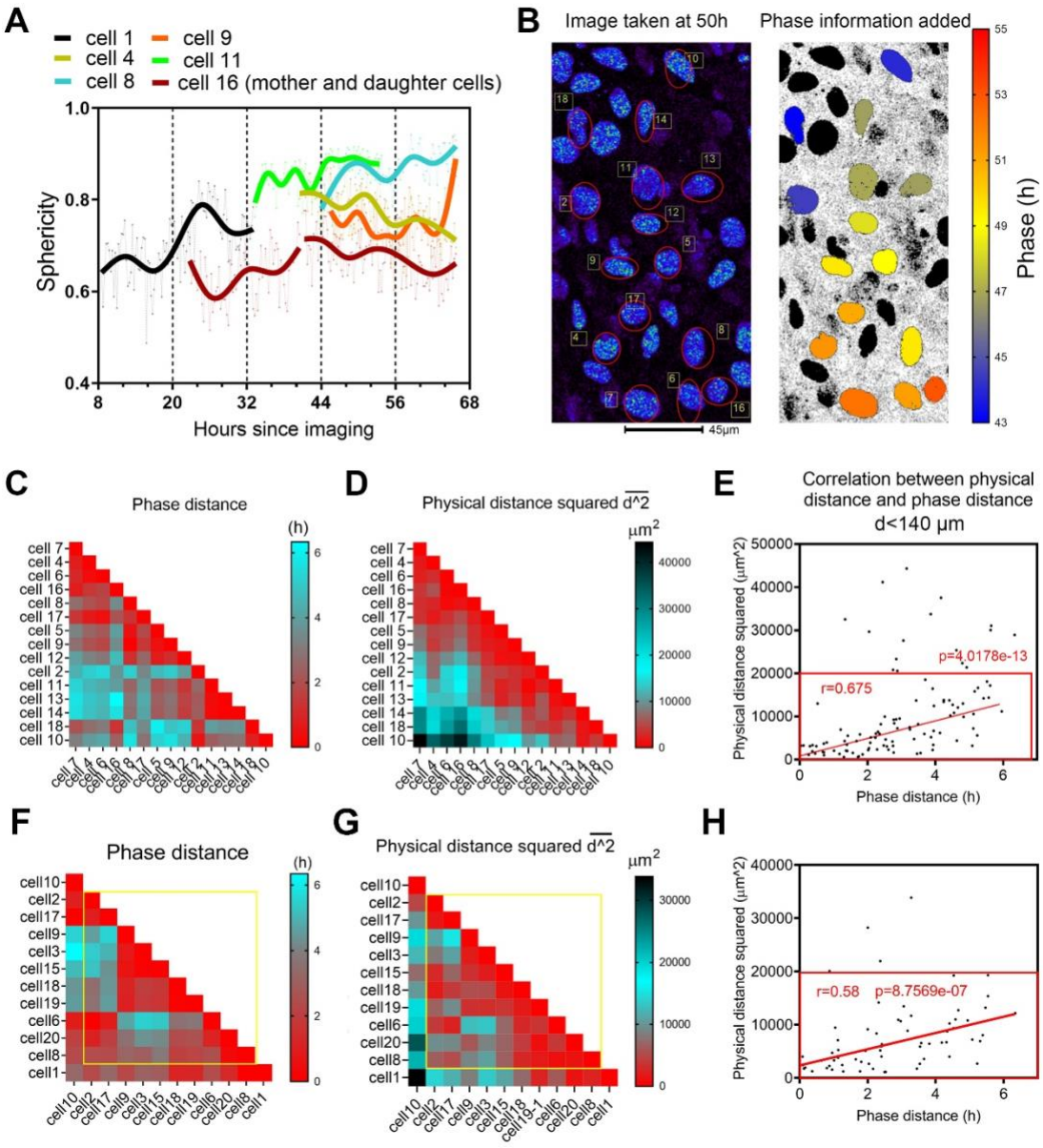

fig. S3. 12h rhythm of nuclear speckle morphology dynamics exhibits local coupling. (**A-E**) GFP::SC35 MEFs were subject to time lapse imaging without serum synchronization. Quantification of temporal sphericity from single MEFs (**A**). Representative image taken at hour 50 showing the physical location (left) and phase heat map (right) of different cells (**B**). Matrix showing the phase distance (**C**) and the square of physical distance (**D**) of different pairs of cells. Scatter plot of phase distance and the square of physical distance for different pairs of cells. Note that a positive correlation only exist for cells that are within 140 μm distance of each other. Pearson correlation coefficient *r* and p value that *r* is significantly larger than zero are shown for cells within 140 μm distance of each other (**E**). (**F-H**). An independent experiment showing similar data as C to E.

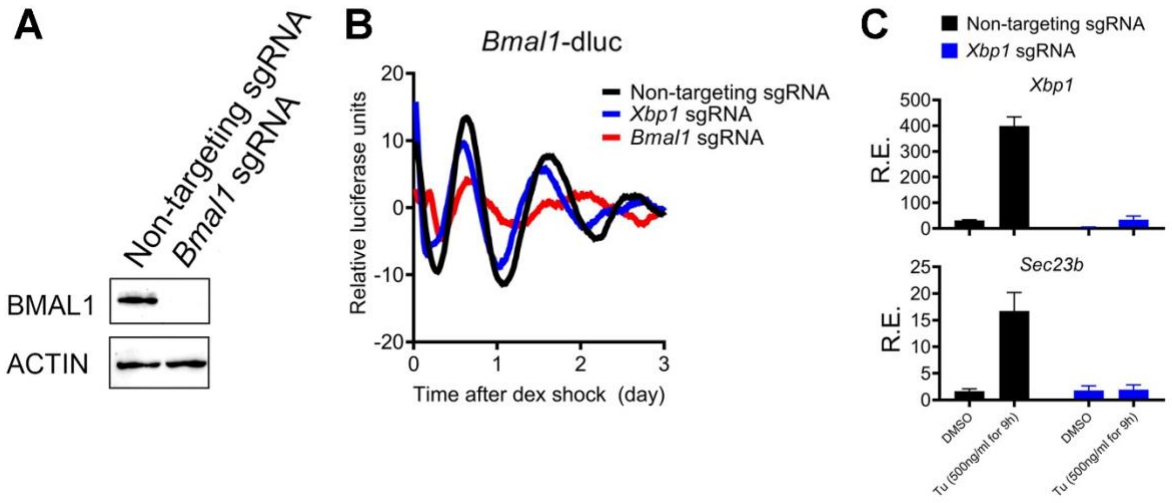

fig. S4. CRISPR/CAS9-mediated ablation of BMAL1 and XBP1 is successful in MEFs. (**A**) Western blot analysis of BMAL1 in GFP::SC35 MEFs expressing non-targeting or *Bmal1* sgRNA. (**B**) Real-time luminescence analysis of *Bmal1-dluc* MEFs post 100nM Dex treatment. Representative detrended traces of luminescence recordings from MEFs expressing non-targeting, *Bmal1* or *Xbp1* sgRNA. (**C**) qPCR analysis of *Xbp1* and UPR gene *Sec23b* in response to tunicamycin (Tu) treatment in GFP::SC35 MEFs expressing non-targeting or *Xbp1* sgRNA. The complete abolishment of *Sec23* induction by Tu indicates the functional ablation of XBP1 protein. Data: Mean ± SEM.

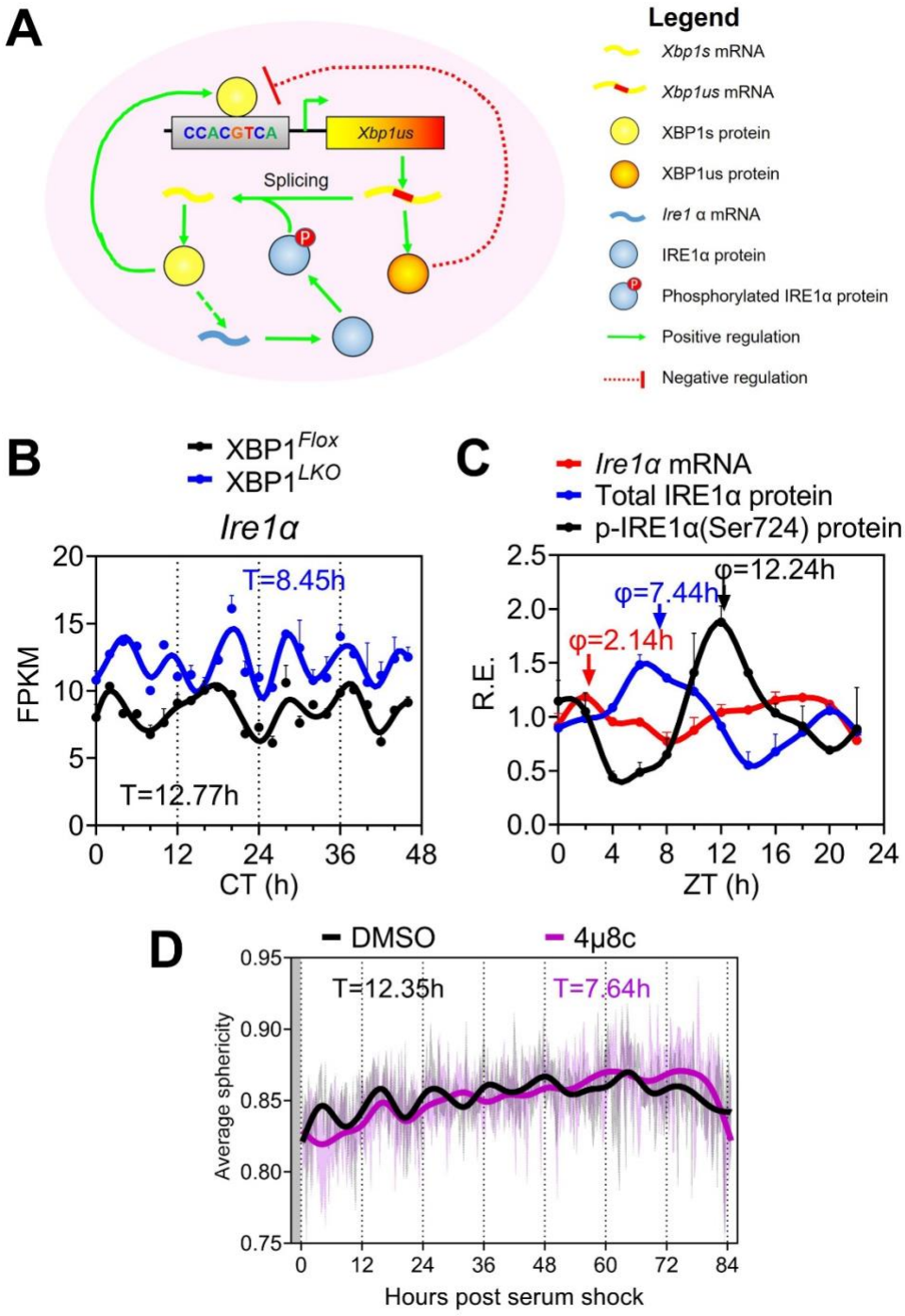

fig. S5. IRE1α inhibition impairs the 12h rhythm of nuclear speckle morphology change. (**A**) The regulatory network of 12h oscillator as previously proposed (*7*). XBP1s transcriptionally activates its own expression (*Xbp1us*) by binding to its own promoter (solid green arrow), whereas XBP1us has been previously shown to inhibit XBP1s transcriptional activity (*58*) (dashed red line). *Ire1α* mRNA exhibits an XBP1s-dependent 12h rhythm, thereby putting itself both downstream and upstream of XBP1s (solid green arrows). More importantly, since elevated IRE1α expression can increase *Xbp1* splicing in the absence of exogenous ER stress stimuli (*59*), mathematically,

it suggests that the 12h oscillator can, in theory, function without input on protein (mis)folding states from the ER. What remains unclear is whether XBP1s can directly transcriptionally regulate *Ire1α* mRNA via binding to its promoter or requires intermediate transcription factor(s) (dashed green arrow). (**B**) RNA-seq of hepatic *Ire1α* in XBP1^{FLOX} and XBP1^{LKO} mice, as reported in (*6*). (**C**) Quantification of hepatic total and phosphorylated IRE1α protein at different circadian time as reported in (*3*), overlaid with *Ire1α* RNA-seq data. Delayed phases from *Ire1α* mRNA to total IRE1α protein to phosphorylated IRE1α protein supports the model depicted in A. Data: Mean ± SEM. (**D**) Temporal sphericity of serum-synchronized GFP::SC35 MEFs treated with DMSO control or 10μM 4μ8c (average sphericity was calculated from each image that contains at least 15 cells, 3~4 images were taken per treatment; light area: mean ± SEM; solid line: spline fit), Gray areas indicates two hours of serum shock. Dominant periods from each group were calculated by the eigenvalue/pencil method.

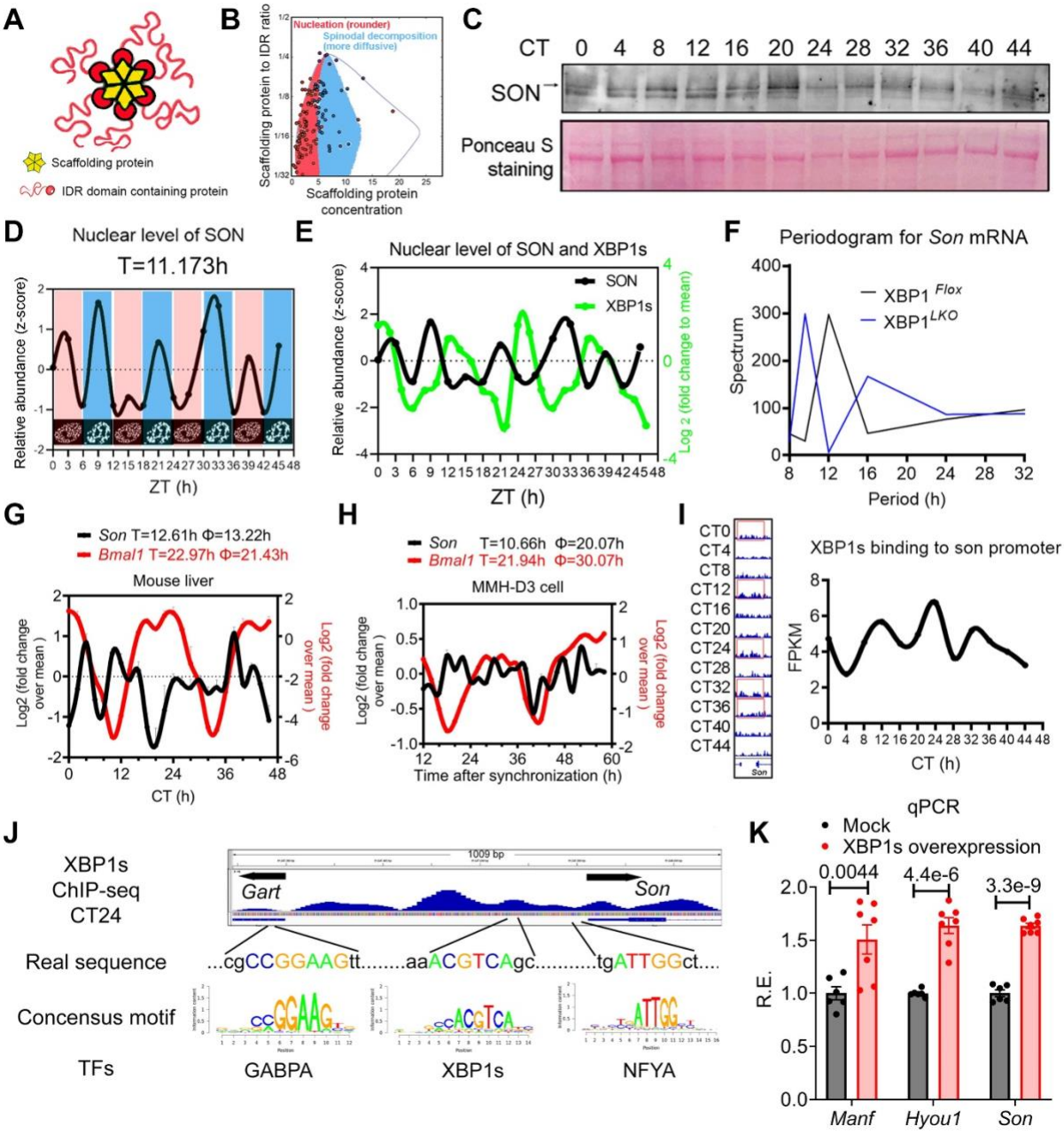

fig. S6. XBP1s regulates 12h rhythm of *Son* expression. (**A**) A cartoon showing the minimal components required for LLPS that include a multivalent 'scaffold' and multiple clients with IDR. (**B**) The phase diagram illustrating the conditions under which LLPS occurs via nucleation (red region) or spinodal decomposition (blue region). Under constant valency condition (the stoichiometry of clients to scaffold in the condensates as illustrated by the y-axis), increasing the concentration of scaffold protein will drive LLPS from nucleation to spinodal decomposition. (**C**) Additional western blot of hepatic SON protein at different CT with 4h resolution. (**D**) Relative abundance of hepatic SON at different zeitgeber time (ZT) superimposed with nuclear speckle morphology cartoons as reported in (*9*). (**E**) Relative abundance of hepatic SON protein superimposed with relative level of XBP1s protein quantified by western blot. (**F**) Periodogram of hepatic *Son* mRNA oscillation in XBP1^{Flox} and XBP1^{LKO} mice. (**G, H**) Log_2 transformed expression

of temporal *Son* and *Bmal1* in mouse liver (**G**) and MMH-D3 cells (**H**) with calculated period and phase by the eigenvalue/pencil method. (**I**) Snapshot (left) and quantification (right) of XBP1s ChIP-Seq signal at *Son* promoter at different CTs in XBP1^{Flox} mice as reported in (*6*). (**J**) Snapshot of XBP1s ChIP-Seq signal at CT24 at *Son* promoter as well as identified DNA binding motifs for GABPA, XBP1s and NFYA transcription factors. (**K**) qPCR analysis of *Son*, *Hyou1* and *Manf* expression in MEFs mock-transfected or transfected with Flag-XBP1s-PHAGE plasmid as previously described (*4*). Data: Mean ± SEM.

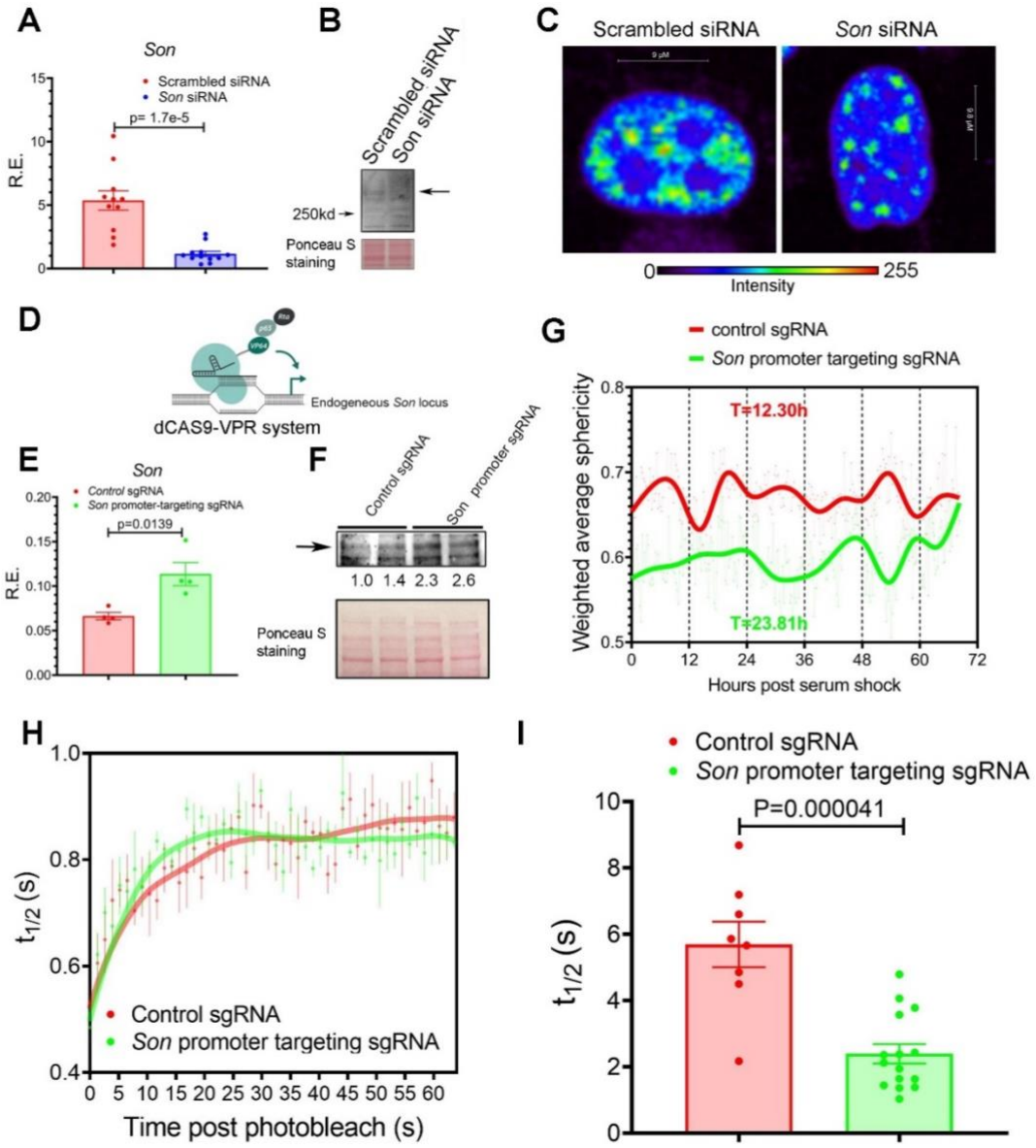

fig. S7. SON positively modulates nuclear speckle fluidity. (**A, B**) qPCR (**A**) and Western blot (**B**) of Son level in MEFs transfected with scrambled or *Son* siRNA. (**C**) Representative image of GFP::SC35 MEFs transfected with scrambled or *Son* siRNA. (**D-F**) Illustration of using the dCAS9-VPR system to transactivate endogenous *Son* gene expression (**D**). qPCR (**E**) and western blot (**F**) of Son level in MEFs stably expressing dCAS9-VPR and control or *Son* promoter-targeting sgRNA. (**G-I**) GFP::SC35 MEFs were stably expressing dCAS9-VPR and control or *Son* promoter-targeting sgRNA. After serum synchronization, weighted average sphericity were directly calculated from 10 to 30 cells at any given time with spline fit also shown, and periods were calculated by the eigenvalue/pencil method (**G**). FRAP analysis with representative recovery curve (**H**) (data showing quantification from 3 speckles per cell; mean ± SEM for each point; solid line: LOWESS fit) and quantified recovery half-life (**I**).

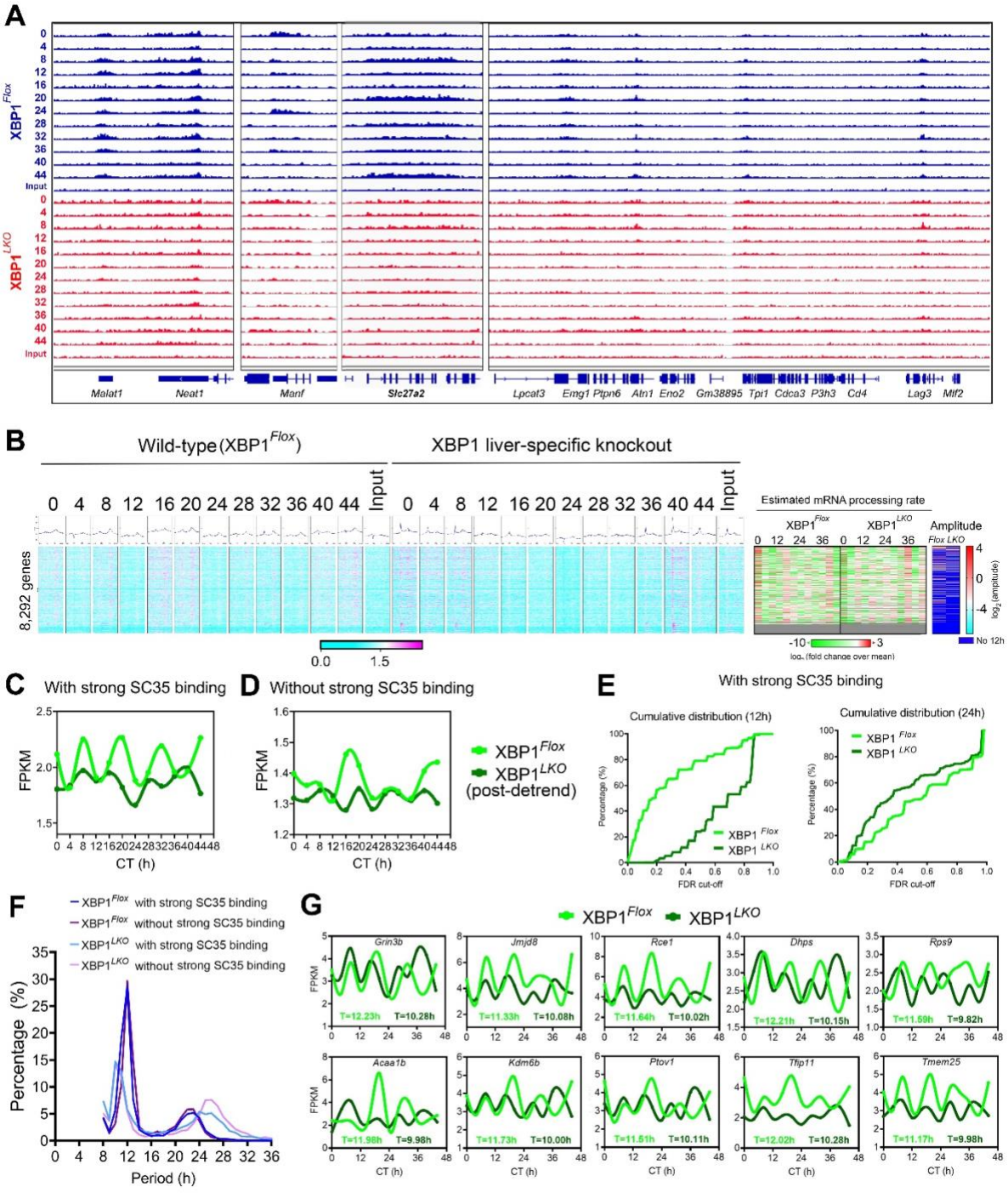

fig. S8. XBP1s regulates 12h nuclear speckle-chromatin interactions. (**A**) Snapshot of target genes selected for alignment of hepatic SC35 binding sites at different CTs in XBP1^{Flox} and XBP1^{LKO} mice. (**B**) Heat map of temporal SC35 as well as input signal for 8,292 genes that are below detection threshold for SC35 peak-calling algorithms in XBP1^{Flox} and XBP1^{LKO} mice from 10kb upstream of transcription start site (TSS) to 10kb downstream of transcription termination site (TTS) for each gene, aligned with the heat map of estimated mRNA processing rate (with amplitude for 12h rhythm) at different CT in XBP1^{Flox} and XBP1^{LKO} mice. (**C, D**) Quantification of

average integrated SC35 signal over gene bodies of 5,365 genes (**C**) and 8,292 genes (**D**) in XBP1^{Flox} and XBP1^{LKO} mice at different CTs. The quantification in XBP1^{LKO} mice is performed on data after polynomial detrend. (**E**) Cumulative distribution of the percentage of 12h (top) or 24h SC35 integrated signal (bottom) under different FDR cut-offs in both XBP1^{Flox} and XBP1^{LKO} mice from the RAIN analysis. Only those 5,365 genes with strong SC35 binding are included in the analysis. (**F**) Period distributions of all dominant oscillations (oscillation with the largest amplitude for each gene) of nuclear speckle-chromatin interactions uncovered by the eigenvalue/pencil method for 5,365 genes with strong SC35 binding and 8,292 genes without strong SC35 binding in both XBP1^{Flox} and XBP1^{LKO} mice. (**G**) Quantification of integrated SC35 signal over gene bodies for selected genes with ~12h nuclear speckle-chromatin interaction dynamics converted to ~10h ones with hepatic ablation of XBP1. The periods (calculated by the eigenvalue/pencil method) of nuclear speckle-chromatin interaction dynamics were shown for each gene in XBP1^{Flox} and XBP1^{LKO} mice.

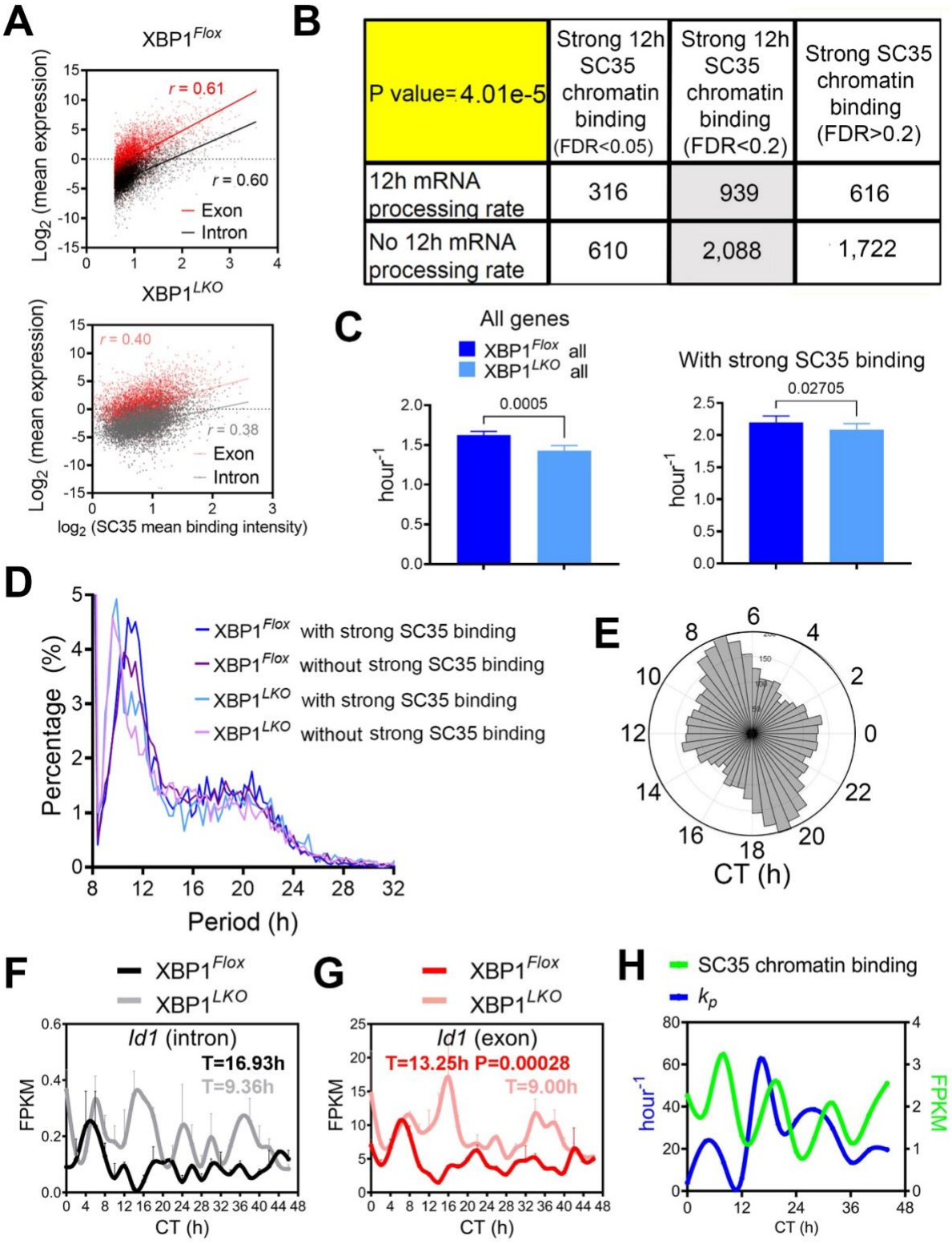

P value= 4.01e-5	Strong 12h SC35 chromatin binding (FDR<0.05)	Strong 12h SC35 chromatin binding (FDR<0.2)	Strong SC35 chromatin binding (FDR>0.2)
12h mRNA processing rate	316	939	616
No 12h mRNA processing rate	610	2,088	1,722

fig. S9. XBP1s regulates 12h mRNA processing rate. (**A**) Scatter plot showing the relationship between $\log_2$ transformed values of pre (intron-mapping) and mature (exon-mapping) mRNA level and integrated SC35 ChIP-seq signal over gene bodies for 5,365 genes in XBP1^{Flox} (top) and

XBP1^{LKO} (bottom) mice. Pearson correlation coefficients *r* are further shown. (**B**) A table summarizing the number of genes with or without strong 12h SC35 signal and 12h mRNA processing rates under different FDR cut-off (from RAIN analysis) in XBP1^{Flox} mice. P value from chi-squared test indicating genes with 12h SC35 binding are also strongly associated with 12h mRNA processing rates. (**C**) Estimated mRNA processing rate for all (top) and 5,365 genes with strong SC35 signal (bottom) in both XBP1^{Flox} and XBP1^{LKO} mice. (**D**) Period distributions of all dominant oscillations (oscillation with the largest amplitude for each gene) of estimated mRNA processing rates uncovered by the eigenvalue/pencil method for 5,365 genes with strong SC35 binding and 8,292 genes without strong SC35 binding in both XBP1^{Flox} and XBP1^{LKO} mice. (**E**) Polar histogram demonstrating the phase distributions of 12h rhythmic mRNA processing rates for all genes in XBP1^{LKO} mice. (**F-H**) Temporal expression of *Id1* at the pre-mRNA, mature mRNA level in XBP1^{Flox} (**F**) and XBP1^{LKO} (**G**) mice, and integrated SC35 gene body signal and mRNA processing rate in XBP1^{Flox} mice (**H**). Data: Mean ± SEM.

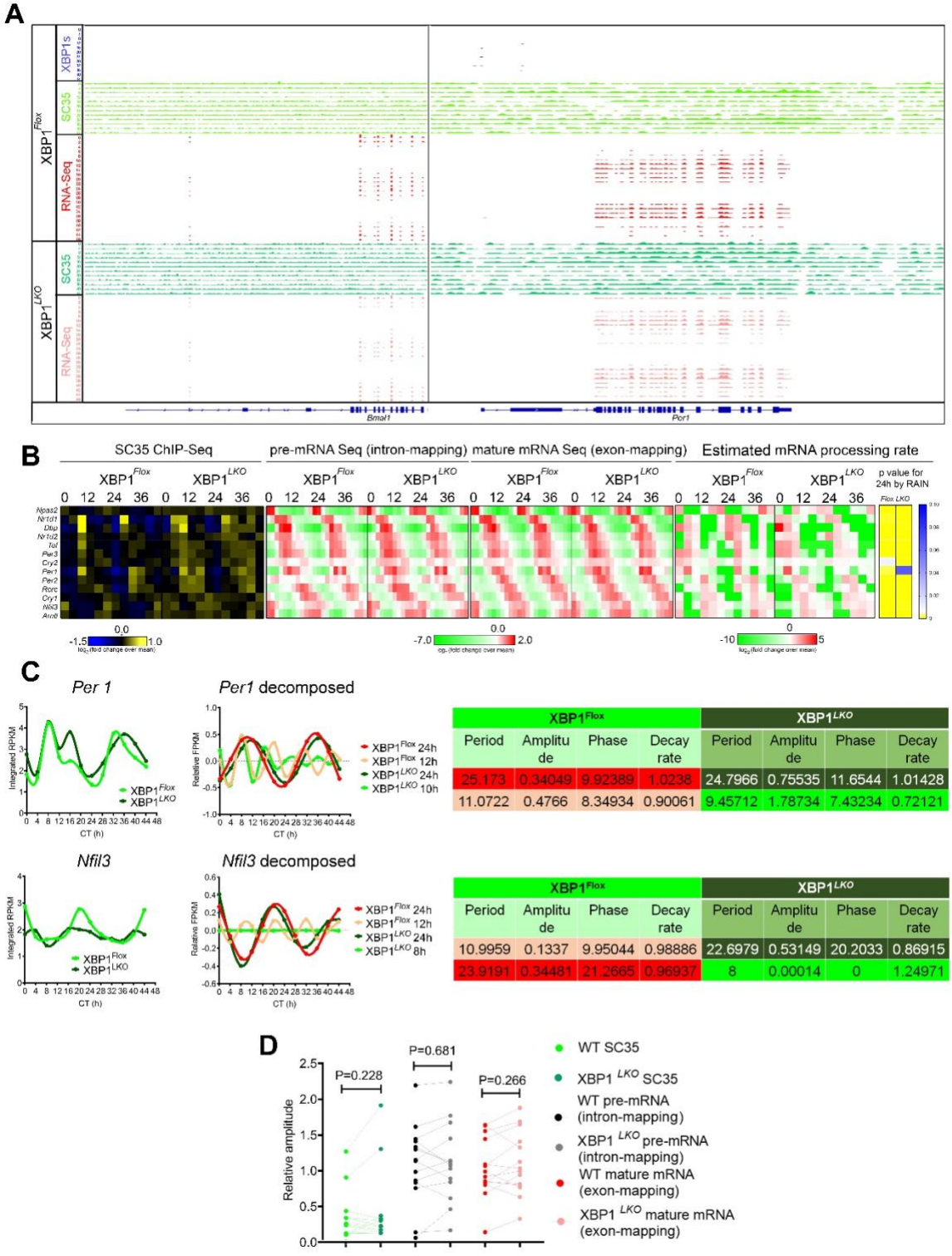

	XBP1Flox				XBP1LKO			
	Period	Amplitude	Phase	Decay rate	Period	Amplitude	Phase	Decay rate
Per1	25.173	0.34049	9.92389	1.0238	24.7966	0.75535	11.6544	1.01428
Per1 decomposed	11.0722	0.4766	8.34934	0.90061	9.45712	1.78734	7.43234	0.72121
Nfil3	10.9959	0.1337	9.95044	0.98886	22.6979	0.53149	20.2033	0.86915
Nfil3 decomposed	23.9191	0.34481	21.2665	0.96937	8	0.00014	0	1.24971

fig. S10. 12h nuclear speckle-chromatin interactions are dispensable for 24h core circadian clock gene expression. (**A**) Snapshot of core circadian clock genes selected for alignment of hepatic XBP1s, SC35 binding and RNA-Seq tracks at different CTs in XBP1^{Flox} and XBP1^{LKO} mice. (**B**) Heat maps of relative integrated SC35 binding signal over gene bodies, pre-mRNA and mature mRNA expression, and estimated mRNA processing rate (with p value for having a 24h

rhythm by RAIN) at different CT in XBP1^{Flox} and XBP1^{LKO} mice for core circadian clock genes. (**C**) Quantification of integrated SC35 signal over gene bodies for *Per1* and *Nfil3* (left), top two decomposed oscillations (middle) and the table showing the detailed parameters of different oscillations (right) by the eigenvalue analysis. Note the 24h components of rhythmic nuclear speckle-chromatin interaction are comparable between XBP1^{Flox} and XBP1^{LKO} mice, but the 12h component is abolished in XBP1^{LKO} mice. (**D**) Quantification of the relative amplitude of 24h SC35 ChIP-seq signal, and pre and mature mRNA oscillation for core circadian clock genes in XBP1^{Flox} and XBP1^{LKO} mice.

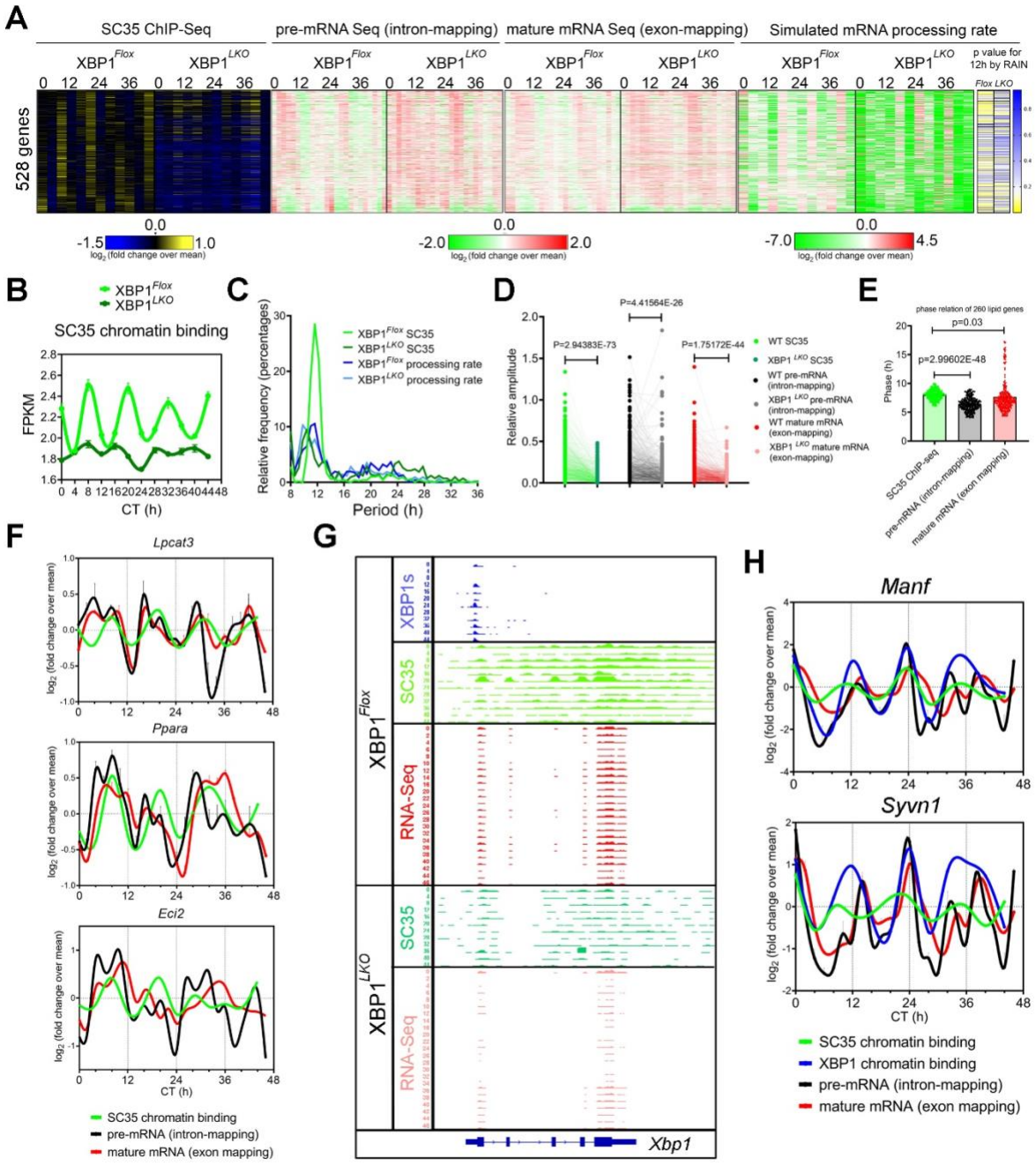

fig. S11. 12h nuclear speckle-chromatin interactions regulate UPR gene expression. (**A**) Heat maps of relative integrated SC35 binding signal over gene bodies, pre-mRNA and mature mRNA expression, and estimated mRNA processing rate (with p values for having a 12h rhythm by RAIN) at different CTs in XBP1^{Flox} and XBP1^{LKO} mice for 528 genes that exhibit very robust 12h rhythms of nuclear speckle-chromatin interaction as well as 12h rhythms of gene expression in XBP1^{Flox} mice. (**B**) Quantification of average integrated SC35 signal over gene bodies of 528 genes in XBP1^{Flox} and XBP1^{LKO} mice at different CTs. The quantification in XBP1^{LKO} mice is performed on data after polynomial detrend. (**C**) Period distributions of all dominant oscillations (oscillation with the largest amplitude for each gene) of estimated mRNA processing rates and

integrated SC35 signal over gene bodies uncovered by the eigenvalue/pencil method in XBP1^{Flox} and XBP1^{LKO} mice for 528 genes. (**D**) Quantification of relative amplitude of 12h SC35 ChIP-seq signal, and pre and mature mRNA oscillation for 528 genes in XBP1^{Flox} and XBP1^{LKO} mice. If no 12h rhythm was found, then the amplitude is deemed zero. (**E**) Quantification of the phases of 12h rhythmic SC35 signal, pre-mRNA and mature mRNA gene expression in 260 genes enriched in lipid metabolism and PPAR signaling in XBP1^{Flox} mice. Data: Mean ± SEM. (**F**) Relative temporal integrated SC35 binding signal over gene bodies, and pre and mature mRNA level for representative lipid metabolism genes in XBP1^{Flox} mice. (**G**) Snapshot of *Xbp1* locus for alignment of hepatic XBP1s, SC35 binding and RNA-Seq tracks at different CTs in XBP1^{Flox} and XBP1^{LKO} mice. (**H**) Relative temporal integrated SC35 binding signal over gene bodies, and pre and mature mRNA level for two UPR genes in XBP1^{Flox} mice.

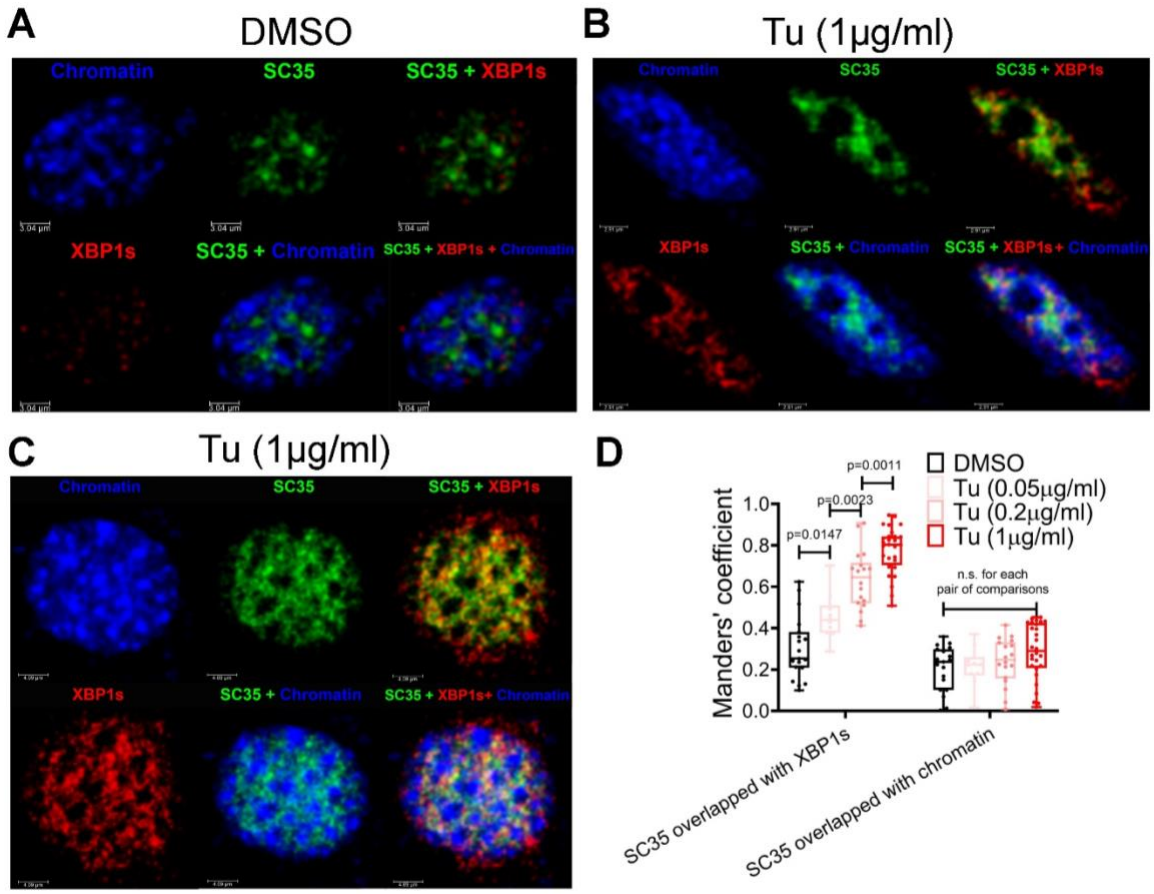

fig. S12. Co-localization of nuclear speckle and XBP1s is observed during UPR. Immunofluorescence of anti-XBP1s (red), GFP signal (green) from GFP::SC35 MEFs and DAPI nuclei staining (blue) as well as merged images of either two or all three channels in GFP::SC35 MEFs treated with increasing concentration of tunicamycin. Representative images from DMSO vehicle control group (**A**) and tunicamycin (1μg/ml) group (two representative images) (**B, C**), and Manders' coefficient quantification (**D**) of co-localization of SC35/XBP1s and SC35/DAPI signals. Box and whiskers plot showing minimum to maximum values.

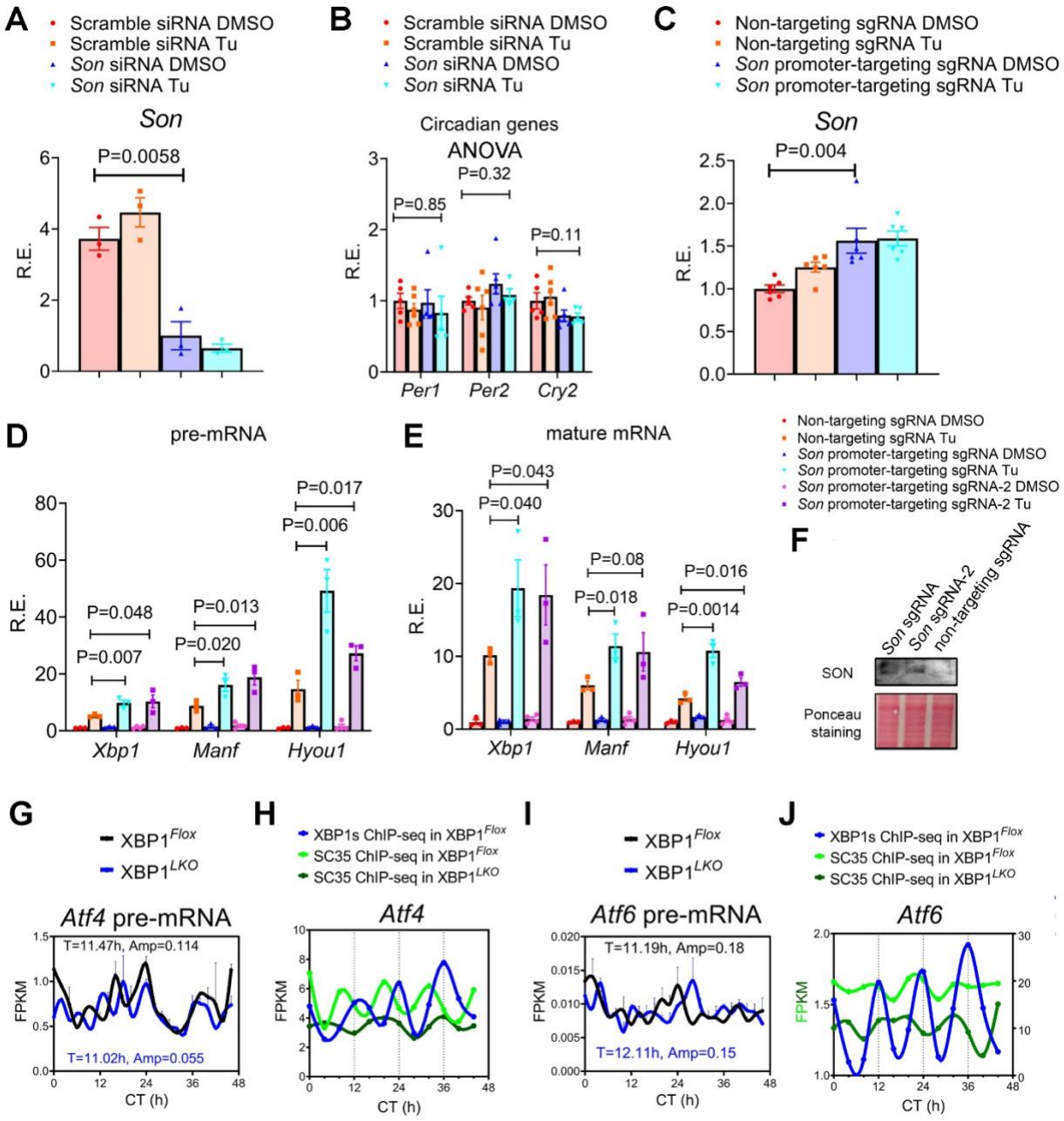

fig. S13. SON transcriptionally amplifies UPR. (**A-C**) MEFs with *Son* siRNA-mediated knocking down (**A, B**) or dCAS9-VPR-mediated stable overexpression of *Son* (**C**) were treated with 100ng/ml of tunicamcyin for 6 hours and qPCR analysis of different genes were performed. (**D-F**) dCAS9-VPR stably expressing MEFs were transiently transfected with non-targeting or two different *Son* promoter-targeting sgRNAs and treated with 100ng/ml of tunicamcyin for 6 hours. qPCR analysis of different genes was performed (**D, E**) and western blot of SON in DMSO group (**F**). (**G-J**) Temporal expression of *Atf4* (**G, H**) *and Atf6* (**I, J**) pre-mRNA level in XBP1^{Flox} and XBP1^{LKO} mice as reported in (*6*), XBP1s ChIP-seq signal in XBP1^{Flox} mice as reported in (*6*) and integrated SC35 gene body signal in XBP1^{Flox} and XBP1 ^{LKO} mice. Data: Mean ± SEM.

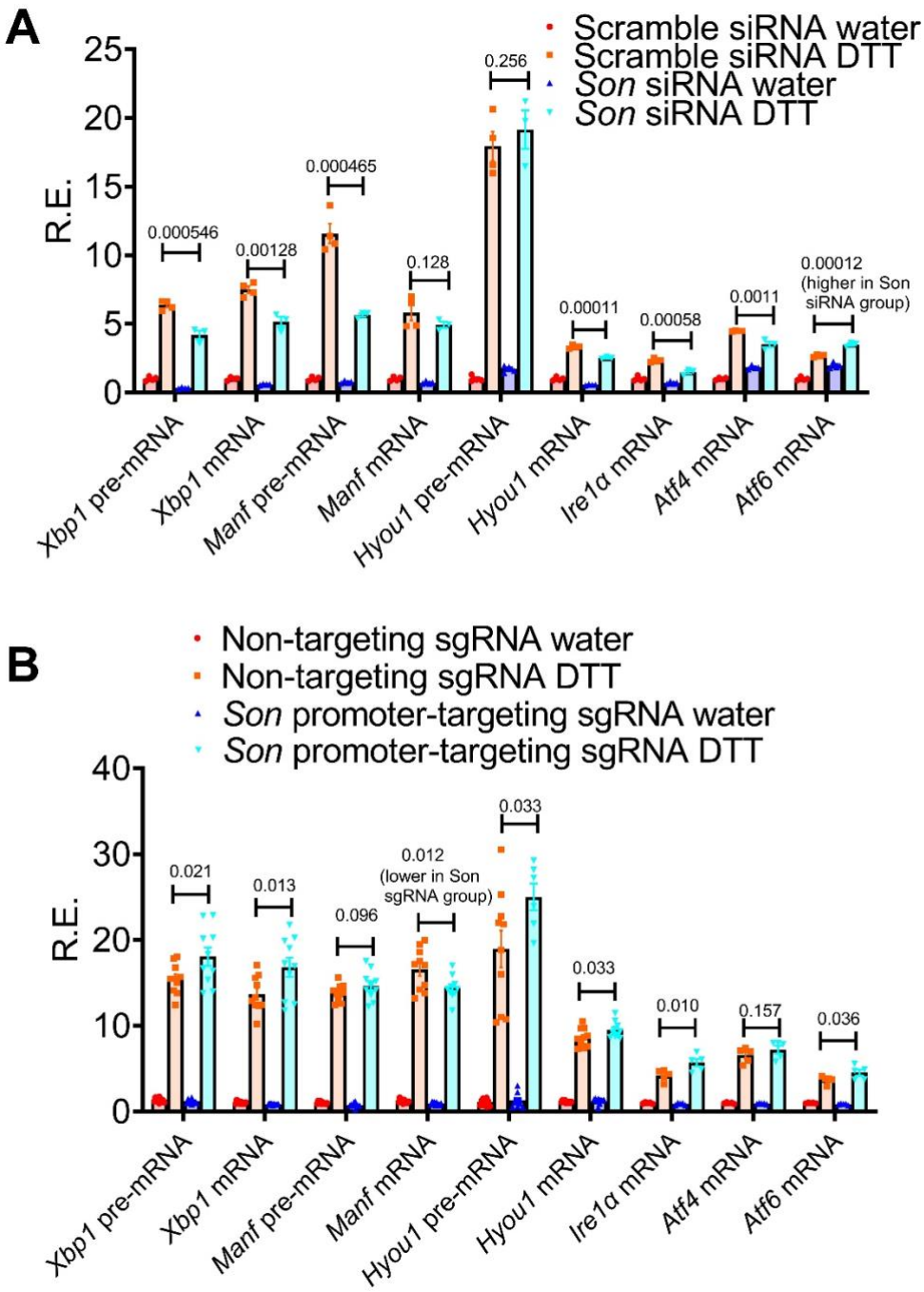

fig. S14. SON transcriptionally amplifies UPR in response to DTT. MEFs with *Son* siRNA-mediated knocking down (**A**) or dCAS9-VPR-mediated stable overexpression of *Son* (**B**) were treated with 1mM DTT for 4~5 hours and qPCR analysis of different genes were performed. Data: Mean ± SEM. Compared with tunicamycin-induced UPR, SON amplifies DTT-induced UPR with less potency, which is likely due to the fact that DTT can strongly activate the ATF6 branch of the UPR rapidly (*60*) and as previously demonstrated, SON has little effects on ATF6 expression.

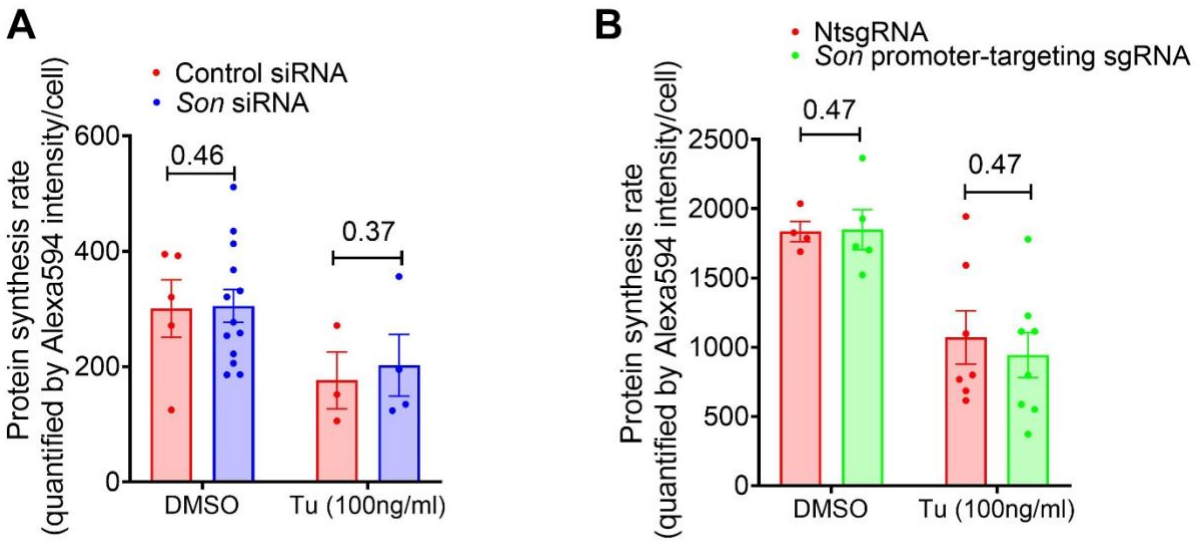

fig. S15. SON does not regulate global protein synthesis rate. Quantification of average protein synthesis rate per cell measured by the incorporation of Alexa594 labelled L-homopropargylglycine in MEFs that were transiently transfected with control or *Son* siRNAs (**A**) or stably expressing dCAS9-VPR and control or *Son* promoter-targeting sgRNAs (**B**) after 6h of DMSO or 100ng/ml Tu treatment. Data: Mean ± SEM.

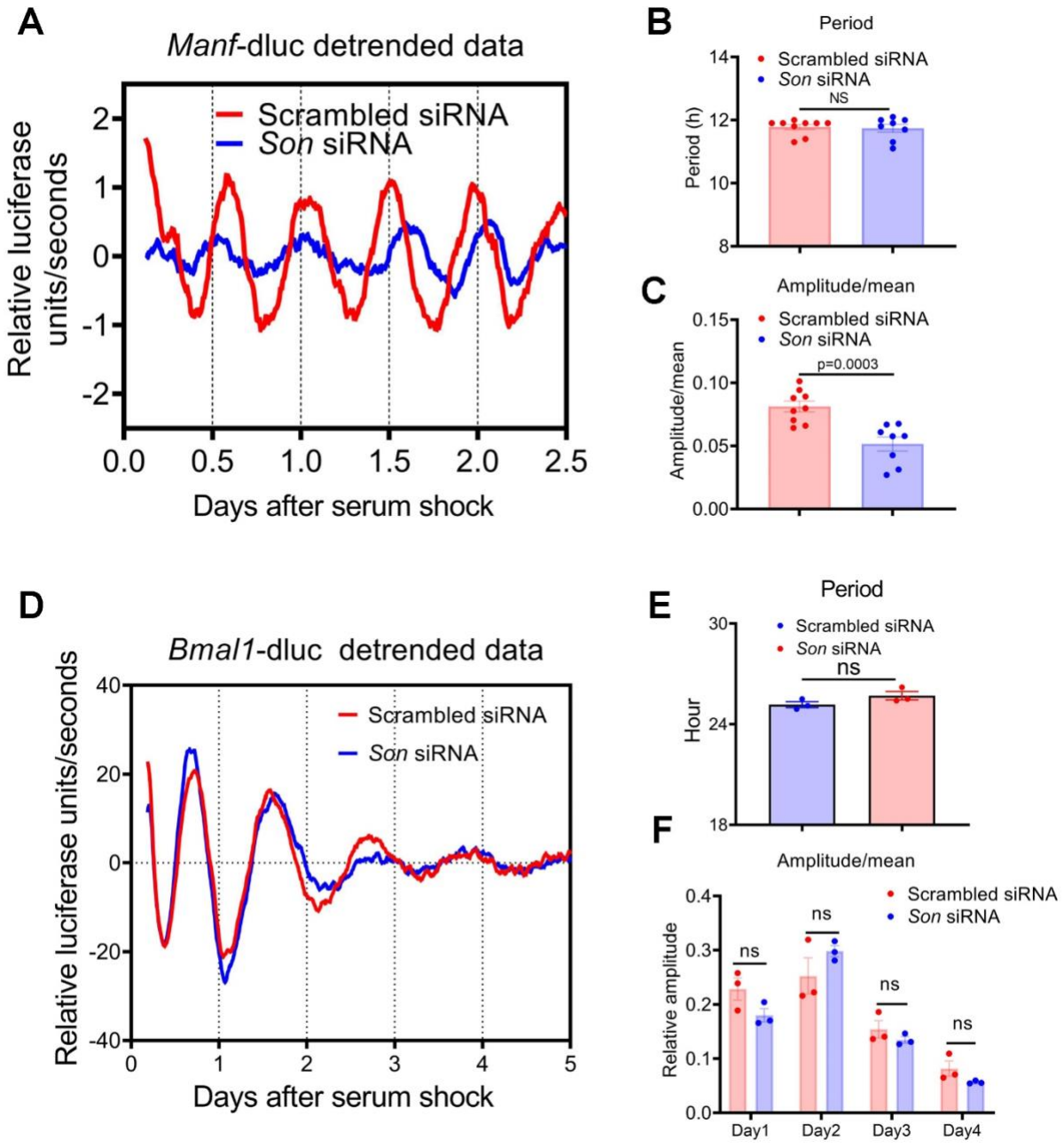

fig. S16. *Son* knocking-down impairs 12h ultradian, but not 24h circadian rhythm in MEFs. (**A-C**) *Manf*-dluc MEFs were transfected with control or *Son* siRNA. Detrend real-time luminescence (**A**), quantified period (**B**) and mean-normalized amplitude (**C**). (**D-F**) *Bmal1*-dluc MEFs were transfected with control or *Son* siRNA. Detrend real-time luminescence (**D**), quantified period (**E**) and mean-normalized amplitude (**F**). Data: Mean ± SEM.

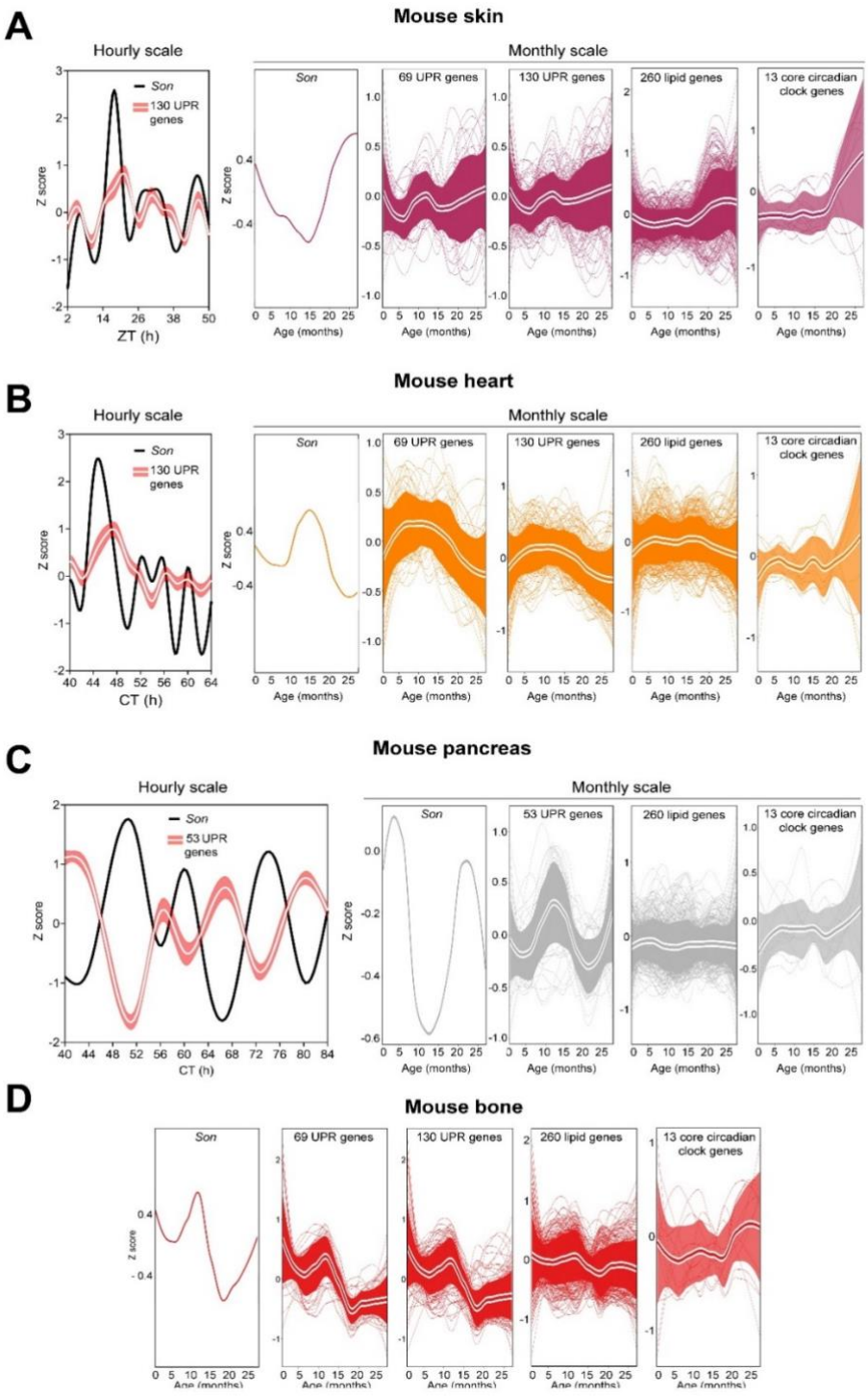

fig. S17. Correlative SON and UPR gene expression dynamics are observed across mouse life span. (**A-D**) Expression of *Son* and UPR genes in a 24~48h window (left) or across the entire mouse life span (right) in different tissues. For the mouse life span data, expression of 260 lipid genes and 13 core circadian clock genes are further shown. To the best of our knowledge, the *Son* or UPR diurnal gene expression status have not been reported in mouse bone. Solid line: mean; shaded area: 95% confidence interval.

table S1. 12h cycling nuclear proteins in mouse liver.
Tab1 All oscillating nuclear proteins idenitifed by the eigenvalue/pencil method (decay rate between 0.8 and 1.2) from Wang et al. (*9*)
Tab 2 All ~12h (period between 10.5h and 13.5h) oscillating nuclear proteins identified by the eigenvalue/pencil method from Wang et al. (*9*)
Tab 3 RAIN analysis on ~12h oscillating nuclear proteins from Wang et al. (*9*)
Tab 4 List and expression of 12h proteins involved in mRNA metabolism, as shown in Figure S1A. from Wang et al (*9*)
Tab 5 All oscillating nuclear proteins idenitifed by the eigenvalue/pencil method (decay rate between 0.8 and 1.2) from Wang et al. (*10*)
Tab 6 All ~12h (period between 10.5h and 13.5h) oscillating nuclear proteins identified by the eigenvalue/pencil method from Wang et al. (*10*)
Tab 7 RAIN analysis on ~12h oscillating nuclear proteins from Wang et al.(*10*)
Tab 8 List and expression of 12h proteins involved in mRNA metabolism, as shown in Figure S1A. from Wang et al. (*10*)

table S2. SC35 ChIP-Seq quantification for 5,365 genes.
Integrated SC35 ChIP-Seq signal over gene bodies (from TSS to TTS) were quantified at different CT for XBP1^{Flox} and XBP1^{LKO} mice for the 5,365 genes. For XBP1^{LKO} mice, quantifications before and after polynomial detrend are shown.

table S3. RAIN analysis for 12h and 24h rhythms of SC35 ChIP-seq signal for 5,365 genes.
Tab 1 12h rhythm identified by RAIN in XBP1^{Flox} mice
Tab 2 12h rhythm identified by RAIN in XBP1^{LKO} mice
Tab 3 24h rhythm identified by RAIN in XBP1^{Flox} mice
Tab 4 24h rhythm identified by RAIN in XBP1^{LKO} mice

table S4. Eigenvalue/pencil analysis of SC35 ChIP-seq signal for all hepatically-expressed genes.
Tab 1 5,365 genes above peak-calling detection threshold in XBP1^{Flox} mice
Tab 2 5,365 genes above peak-calling detection threshold in XBP1^{LKO} mice
Tab 3 8,292 genes below peak-calling detection threshold in XBP1^{Flox} mice
Tab 4 8,292 genes below peak-calling detection threshold in XBP1^{LKO} mice

table S5. FPKM values of RNA-Seq data for exon-mapping reads in XBP1^{Flox} and XBP1^{LKO} mice.
table S6. FPKM values of RNA-Seq data for intron-mapping reads in XBP1^{Flox} and XBP1^{LKO} mice.

movie S1. Time lapse imaging of nuclear speckle morphology change in single GFP::SC35 MEF. The video is 5 frames per second.

movie S2. FRAP video of GFP::SC35 MEF transfected with scrambled siRNA. The video is 5 frames per second.

movie S3. FRAP video of GFP::SC35 MEF transfected with *Son* siRNA. The video is 5 frames per second.